CrossMark

# A DGTD method for the numerical modeling of the interaction of light with nanometer scale metallic structures taking into account non-local dispersion effects

Nikolai Schmitt [a,c], Claire Scheid [a,b], Stéphane Lanteri [a,*], Antoine Moreau [d], Jonathan Viquerat [a]

[a] Inria, 2004 Route des Lucioles, BP 93, 06902 Sophia Antipolis Cedex, France
[b] University of Nice – Sophia Antipolis, Mathematics laboratory, Parc Valrose, 06108 Nice, Cedex 02, France
[c] Technische Universitaet Darmstadt, Institut fuer Theorie Elektromagnetischer Felder (TEMF), Schlossgartenstr. 8, 64289 Darmstadt, Germany
[d] Institut Pascal, Université Blaise Pascal, 24, avenue des Landais, 63171 Aubière Cedex, France

## ARTICLE INFO

## ABSTRACT

The interaction of light with metallic nanostructures is increasingly attracting interest because of numerous potential applications. Sub-wavelength metallic structures, when illuminated with a frequency close to the plasma frequency of the metal, present resonances that cause extreme local field enhancements. Exploiting the latter in applications of interest requires a detailed knowledge about the occurring fields which can actually not be obtained analytically. For the latter mentioned reason, numerical tools are thus an absolute necessity. The insight they provide is very often the only way to get a deep enough understanding of the very rich physics at play. For the numerical modeling of light-structure interaction on the nanoscale, the choice of an appropriate material model is a crucial point. Approaches that are adopted in a first instance are based on local (i.e. with no interaction between electrons) dispersive models, e.g. Drude or Drude–Lorentz models. From the mathematical point of view, when a time-domain modeling is considered, these models lead to an additional system of ordinary differential equations coupled to Maxwell's equations. However, recent experiments have shown that the repulsive interaction between electrons inside the metal makes the response of metals intrinsically non-local and that this effect cannot generally be overlooked. Technological achievements have enabled the consideration of metallic structures in a regime where such non-localities have a significant influence on the structures' optical response. This leads to an additional, in general non-linear, system of partial differential equations which is, when coupled to Maxwell's equations, significantly more difficult to treat. Nevertheless, dealing with a linearized non-local dispersion model already opens the route to numerous practical applications of plasmonics. In this work, we present a Discontinuous Galerkin Time-Domain (DGTD) method able to solve the system of Maxwell's equations coupled to a linearized non-local dispersion model relevant to plasmonics. While the method is presented in the general 3D case, numerical results are given for 2D simulation settings.

© 2016 Elsevier Inc. All rights reserved.

---

* Corresponding author.
  *E-mail address:* Stephane.Lanteri@inria.fr (S. Lanteri).

# 1. Motivations and objectives

## 1.1. Physical background

Nanometer scale (or even sub-nanometer scale) metallic or metallo-dielectric devices illuminated at optical frequencies demonstrate interesting features that are increasingly exploited in the area of nanophotonics and plasmonics [1–4]. To be able to understand and make use of these enhanced properties, an appropriate modeling is required, in particular to describe the reaction of the electrons in the metal subjected to an incident electromagnetic wave.

Classically, the response of the electron gas is given by Drude's model. Drude's model neglects mutual electron interactions and the polarization current is proportional (in the frequency domain) to the electric field at any spatial position. Hence, the metal behaves like a regular local dielectric medium. The space–time evolution of this polarization is then governed by a set of differential equations which is itself linearly coupled to the classical set of Maxwell's equations.

At the scales and frequencies considered in the recent plasmonic research, the classical description of the electron response, i.e. Drude-like models, is not sufficient. A first step towards an improved model is the inclusion of the mutual repulsion between electrons which can be done by using a hydrodynamic model [5]. Such a model links the effective polarization to the electric field. In this case, the equations governing the evolution of the polarization current are partial differential equations. This leads to the fact that the behavior of the electron gas does not only depend on the field at the considered position (otherwise the response would be deemed local) but also on the neighboring field distribution (making the response non-local). Such a phenomenon is called spatial dispersion. This type of spatially dispersive model is at the heart of the study proposed here. Recent experiments [6,7] as well as theoretical works [8,9] have actually brought forward the idea that the non-local response of the metal and its impact on the global optical response of the structure could be accurately described by such a model.

One of the main setups explaining how a structure can be sensitive to spatial dispersion is light propagation in gaps smaller than 50 nm commonly referred as gap-plasmon. A gap-plasmon is a mode that is able to reach very short effective wavelength [10] if the gap width sufficiently decreases. As the effective wavelength gets closer to the free mean path of electrons in the metal, the influence of spatial dispersion is more and more important [8,11,12]. This can be expected to occur for gaps that are typically smaller than 5 nm. When the size of the gap is smaller than 1 nm, then the slight spill-out of the electron gas outside of the metal has to be taken into account [13]. Above that threshold, however, the optical response is not affected by the spill-out effect, since its typical spatial scale is around 0.2 nm [14]. Below those scales, other models should be considered [5,15]. For gaps lager than 1 nm, hard-wall boundaries, as they have been used in the present work, are expected to lead to sufficiently accurate results regarding the overall physical precision and appropriateness of the model.

## 1.2. Numerical modeling issues

In the field of computational nanophotonics, there is currently a need for efficient and accurate numerical methodologies since the geometries, scales and propagation media can be rather complex. In the literature, a large number of studies are devoted to FDTD (Finite Difference Time-Domain) type discretization methods based on Yee's scheme. Despite their numerous advantages (efficiency and easy implementation), these FDTD methods poorly perform when facing the modeling difficulties that are inherent to nanophotonic applications, in particular in the presence of curved geometries. Indeed, the stair-casing effect resulting from the use of a cartesian grid notably degrades the accuracy of these FDTD methods[1] [16]. Numerical methods based on unstructured and possibly non-conforming meshes[2] are particularly appealing in this context. This is especially the case for approaches based on a Discontinuous Galerkin (DG) formulation. So-called DGTD methods mix the best of finite element and finite volume type discretization methods. They are based on a local formulation on each mesh element, while the continuity constraint at the element boundaries is relaxed. Hence, an appropriate treatment of inter-element boundary integrals appearing in the weak formulation is required. The latter leads to the definition of a numerical trace or numerical flux (in the spirit of finite volume schemes). These DGTD methods are possibly high order and are flexible enough to deal with heterogeneous media and complex geometries. They are especially well-suited to parallel computations for reducing the computational time when simulating three-dimensional problems. DGTD methods for solving the system of time-domain Maxwell's equations have been extensively studied in the last 10 years, following the seminal work of Hesthaven and Warburton [17]. In a more recent work, Li and Hesthaven [18] develop a nodal DGTD method for solving the time-domain Maxwell's equations when metamaterials are involved. The development of DGDT methods in the nanophotonic area is still limited but one can notice a growing interest in this direction (see e.g. [19–21]). All these studies adopt a diffusive DGTD formulation based on upwind numerical fluxes. Besides, several studies have already been conducted regarding the development of DGTD methods for dispersive media such as [22–24]. Furthermore one can find more studies focused on numerical analysis aspects concerning dispersive media [25,26]. In the framework of non-dissipative formulations [27], a DGTD method able to treat local dispersive models for metallic structures has recently been designed and studied in [28].

---

[1] In the absence of a specific adaptation of the original FDTD formulation allowing the use of a body-fitted cartesian grid.

[2] The term *non-conforming meshes* is used by means of meshes with hanging nodes.

### 1.3. Objectives of this study and related works

A vast majority of the studies concerned with the numerical modeling of the linearized fluid model that governs the non-local dispersion behavior of metals, are devoted to frequency domain approaches (see e.g. [29–32] and references therein) in a Finite Difference or Finite Element framework. The present work is concerned with the design and numerical study of a DGTD method for the non-local model in time-domain. The problem statement in the three-dimensional (3D) case and the corresponding initial and boundary value problem are described in section 2. As in [27,28,24], the proposed DGTD formulation combines a centered numerical flux with a second order leap-frog time integration scheme. This is detailed in section 3. From the theoretical viewpoint, we conduct a stability analysis of the resulting DGTD method and show that the method is stable under a CFL condition. Finally, this DGTD method is implemented in the two-dimensional (2D) case for the transverse electric mode formulation of Maxwell's equations and some validation test problems are presented. This is the subject of section 4.

## 2. Problem statement and notations

This section introduces the underlying physics and models this work is based on. Beginning with Maxwell's macroscopic equations for electrodynamics we subsequently present the linearized non-local dispersion model which is appropriate for a certain dimensional range of nanophotonic devices where non-local effects in terms of electron interactions have to be taken into account. If those dimensions become even smaller down to a level where the quantum mechanics (QM) behavior of electrons, i.e. tunneling through regions that are classically forbidden occur, even semi-classical non-local models are not sufficient anymore and full QM descriptions are required [14,13]. In this work, we will not consider dimensions where the latter descriptions are necessary and though stick to effects that can be appropriately modeled with a so called non-local hydrodynamic fluid model with hard-wall boundary conditions [8].

As this work is mainly concerned with non-local dispersion models, the local dispersion effects are kept shortly while focusing on the physics which cause the non-local dispersion of metals in a frequency regime around and beyond a characteristic frequency called plasma frequency. Then, the hydrodynamic modeling that governs the electron coupling is presented and we derive the linearized fluid model from a general non-linear hydrodynamic model. Maxwell's equations together with the latter mentioned linearized fluid model lead to a new system of Partial Differential Equations (PDEs). In order to characterize this PDE system, we show its hyperbolicity and analyze the energy evolution in time. As the numerical treatment is here restricted to the 2D case (in the sense of a 3D problem with an invariance in one given direction), it appears that non-local effects do only occur in the so called Transverse Electric (TE) mode and thus the Transverse Magnetic (TM) mode can be left out [33]. This section closes with a proper definition of the here considered boundary value problem and a comparison of the local and non-local models. Additionally, a rescaled form of the model problem is derived for the purpose of the implementation.

### 2.1. The system of Maxwell's equations

The complete set of macroscopic Maxwell's equations describing the spatio-temporal evolution of electromagnetic waves is given in differential form by (see for example [34])

$$\nabla \times \mathbf{E} = -\partial_t \mathbf{B}, \quad \nabla \times \mathbf{H} = \partial_t \mathbf{D} + \mathbf{J}, \tag{1a}$$

$$\nabla \cdot \mathbf{D} = \rho, \quad \nabla \cdot \mathbf{B} = 0, \tag{1b}$$

with $\mathbf{r} \in \mathbb{R}^3$, $t \in \mathbb{R}^+$, $\mathbf{E}, \mathbf{D}, \mathbf{H}, \mathbf{B}, \mathbf{J} : \mathbb{R}^3 \times \mathbb{R} \mapsto \mathbb{R}^3$ and $\rho : \mathbb{R}^3 \times \mathbb{R} \mapsto \mathbb{R}$; where $\nabla \times \mathbf{A}$, and $\nabla \cdot \mathbf{A}$ respectively denote the curl and the div operator applied to a vector field $\mathbf{A}$. Here, $\mathbf{E}$ and $\mathbf{H}$ represent the electric and magnetic field, respectively. The magnetic flux density is denoted by $\mathbf{B}$ and the electric displacement and current density respectively by $\mathbf{D}$ and $\mathbf{J}$, and the charge density by $\rho$. These equations are supplemented by material laws linking $\mathbf{D}$ to $\mathbf{E}$ and $\mathbf{B}$ to $\mathbf{H}$ through the introduction of

$$\mathbf{D} = \varepsilon_0 \mathbf{E} + \mathbf{P}, \quad \mathbf{B} = \mu_0 \mathbf{H} + \mathbf{M}. \tag{2}$$

Here, $\varepsilon_0$ and $\mu_0$ are the vacuum permittivity and permeability, $\mathbf{P} : \mathbb{R}^3 \times \mathbb{R} \mapsto \mathbb{R}^3$ the polarization and $\mathbf{M} : \mathbb{R}^3 \times \mathbb{R} \mapsto \mathbb{R}^3$ the magnetization. Throughout the following derivations non-magnetic dispersive materials will be assumed because all concepts are applied to non-magnetic metallic structures. The magnetic polarization will thus be considered to be zero. Furthermore, the polarization $\mathbf{P}$ can be split into different contributing parts. Since metals consist of a rigid ion grid that is built of positive ion cores together with the locally fixed bound electrons (d-band) and the freely moving valence electrons (s-band), the polarization can be split in two parts: the background polarization $\mathbf{P}_\infty$ [35] governing the influence of the background electrons and $\mathbf{P}_f$ which models the currents in the free electron gas.

### 2.2. Nanoplasmonics

Resonant nanoparticles are of increasing importance for their foreseen applications in science and technology. Their optical response can only be correctly understood if plasmonic effects are taken into account. This is justified by the range of

the electromagnetic skin depth being of the particle's size. The electromagnetic fields penetrate in noble metals up to 25 nm whatever the wavelength. This skin depth gives a typical size for which the plasmonics nature of metallic structures has to be considered to understand their properties. Metallic regions actually contain a plasma, whose electromagnetic response is in opposition to the incoming field. This is usually described by a negative permittivity in a local recoil approximation. When the size of a metallic structure gets down to the scale of the skin depth, the fields can completely penetrate the particle and excite resonant oscillations [36]. Even further down, if typical dimensions reach regions where electrons can show their full quantum nature like for sub-nanometer gaps between two metallic walls [37], the hydrodynamic model which is used in this work is not applicable anymore and QM wave functions have to be completely taken into account. As a rule of thumb and often mentioned in the literature [37], plasmonic effects for nanostructures should be taken into account when considered dimensions are in the range of ≈1 nm–15 nm, while the incident field wavelength is usually comparatively large and considered as a plane wave [30].

### 2.3. Hydrodynamic modeling of the electron response

A comprehensive discussion on local dispersion models for metals in nanophotonics is given in [38]. The assumption of an ideal free electron gas on which these models rely, faces its limits when it comes to even smaller geometries with dimensions below tenth of nanometers [31,37]. A cube with an edge length of 10 nm, for instance, would hit the critical regime. But also two thick nanowires being placed narrowly with a gap size in the range of ≈1 nm–5 nm would show a different behavior if electron interactions were considered. Among others, QM codes are available that take the full wave character of electrons into account. Although these solvers provide a very accurate model of the underlying physics, the computational effort is so heavy that it makes the simulation of realistic geometries unaffordable.

Various approaches with the purpose of describing the non-local response can be found in the literature e.g. [39]. Within this work the focus is put on a linearized non-local model in terms of an electron fluid moving against a positive ion background similar to the one fluid description for plasmas [40]. This approach includes inter-electron coupling modeled by a hydrodynamic pressure (Coulomb interactions in a Fermi gas) [41]. As an interesting fact it turns out that starting from the hydrodynamic model, linearizing, and finally neglecting the non-local impact, the resulting polarization is equivalently described as the local Drude model.

#### 2.3.1. The linearized fluid model

Given the electron charge $-e$, its mass $m_e$ and a damping constant $\gamma$, the hydrodynamic model reads:

$$m_e(\partial_t + \mathbf{v} \cdot \nabla)\mathbf{v} = -e[\mathbf{E} + \mathbf{v} \times \mathbf{B}] - m_e \gamma \mathbf{v} - \nabla \left( \frac{\delta g[n]}{\delta n} \right), \tag{3a}$$

together with the continuity equation

$$0 = \partial_t n + \nabla \cdot (n\mathbf{v}), \tag{3b}$$

where $\mathbf{v} : \mathbb{R}^3 \times \mathbb{R} \mapsto \mathbb{R}^3$ represents the fluid velocity, $n : \mathbb{R}^3 \times \mathbb{R} \mapsto \mathbb{R}$ its density and $-e[\mathbf{E} + \mathbf{v} \times \mathbf{B}]$ is the Lorentz force. The last term of the right hand side of (3a) is a quantum pressure term. It is governed by a function of the density denoted $g$, see e.g. [42]. It allows for different models for the electron interactions. Thus, this term has to be considered carefully in order to correctly include the underlying physics. We do not consider the whole non-linear problem as in [43] but linearize the equations around an equilibrium state with zero velocity, no static magnetic field, and constant density denoted $n_0$. We follow [29] and consider the same expression for the quantum pressure. The first order linearized term thus expresses as

$$\beta^2 \frac{1}{n_0} \nabla n, \tag{4}$$

for the quantum pressure. $\beta$ is the quantum related parameter that has to be fixed according to the physics of the problem. Its choice is a crucial point in this model. For the moment, this parameter is left arbitrarily even though it is fairly often set to $\sqrt{3/5}v_F$ using the Fermi velocity $v_F$ [42,5]. Thus for (3a), the linearized equation writes

$$m_e \partial_t \mathbf{v} = -e\mathbf{E} - m_e \gamma \mathbf{v} - m_e \beta^2 \frac{1}{n_0} \nabla n, \tag{5}$$

and for (3b)

$$\partial_t n = -n_0 \nabla \cdot \mathbf{v}. \tag{6}$$

Differentiating (5) with respect to the time $t$, inserting (6) and using $\mathbf{J} = -n_0 e\mathbf{v}$, the current density of the unbound electrons in the fluid yield formally

$$0 = \partial_{tt}\mathbf{J} + \gamma \partial_t \mathbf{J} - \beta^2 \nabla(\nabla \cdot \mathbf{J}) - \omega_p^2 \varepsilon_0 \partial_t \mathbf{E}. \tag{7}$$

Together with Maxwell's equations, the nature of the resulting system of equations is different from a classical local Drude model. While the polarization current was simply described by an ODE (Ordinary Differential Equation) in a local Drude

model see [38], the non-local linearized hydrodynamical model requires the additional solution of a PDE (7). For the rest of this work, we will stick to this formulation.

### 2.3.2. Hyperbolicity of the linearized non-local model

Given a description of the polarization of bound and free electrons, the entire considered physics is modeled by Maxwell's equations for the electrodynamic contribution, the remaining background polarization $\mathbf{P}_\infty$ for the bound electrons, and the Linearized Fluid (LF) model for the free electron gas. This total system of PDE reads

$$\nabla \times \mathbf{H} = \partial_t \mathbf{D},$$
$$\nabla \times \mathbf{E} = -\mu_0 \partial_t \mathbf{H}, \tag{8a}$$
$$\partial_t \mathbf{D} = \varepsilon_0 \varepsilon_\infty \partial_t \mathbf{E} + \mathbf{J},$$
$$\omega_p^2 \varepsilon_0 \partial_t \mathbf{E} = \partial_{tt} \mathbf{J} + \gamma \partial_t \mathbf{J} - \beta^2 \nabla (\nabla \cdot \mathbf{J}), \tag{8b}$$

where all currents are considered as a charge displacement in terms of polarization. We propose to introduce an auxiliary scalar quantity $Q$ in order to transform (8) to a mixed first order PDE system

$$\mu_0 \partial_t \mathbf{H} + \nabla \times \mathbf{E} = 0,$$
$$\varepsilon_0 \varepsilon_\infty \partial_t \mathbf{E} - \nabla \times \mathbf{H} = -\mathbf{J},$$
$$\partial_t \mathbf{J} - \beta^2 \nabla Q = \omega_p^2 \varepsilon_0 \mathbf{E} - \gamma \mathbf{J}, \tag{9}$$
$$\partial_t Q - \nabla \cdot \mathbf{J} = 0,$$

that can be recast in a conservative form

$$\partial_t \mathbb{L} \mathbf{u} + \nabla \cdot \mathbf{F}(\mathbf{u}) = 0, \text{ with } \mathbf{u} = \begin{pmatrix} \mathbf{E} & \mathbf{H} & \mathbf{J} & Q \end{pmatrix}^T. \tag{10}$$

$Q$ is a scalar field and indeed represents the charge density. (10) is a hyperbolic system of PDEs with eigenvalues given $\forall \xi \in \mathbb{R}^3$ with $\xi = (\xi_1, \xi_2, \xi_3)^T$,

$$\lambda(\|\xi\|) = \left\{ 0 \quad 0 \quad 0 \quad 0 \quad -c\|\xi\| \quad -c\|\xi\| \quad c\|\xi\| \quad c\|\xi\| \quad -\beta\|\xi\| \quad \beta\|\xi\| \right\}, \tag{11}$$

with the speed of light $c = 1/\sqrt{\mu_0 \varepsilon_0 \varepsilon_\infty}$ (see [33] for more details on the derivation). Since the underlying physics of the non-local contribution are hidden in the quantum related parameter $\beta$, it is kind of straightforward that the eigenvalues depend on $\beta$. Analogous to the electrodynamic case, the two new eigenvalues that depend on $\beta$ can be interpreted as the speed of hydrodynamic waves. Those waves are the propagating bulk plasmons that occur due to non-locality.

### 2.4. Interface and boundary conditions

Considering the propagation problem (9) on a domain $\Omega$, one has to complement the system of PDEs with boundary and initial conditions. For the Maxwell part, one would propose standard boundary conditions depending on the considered test case (e.g. Perfectly Electrical Conductor (PEC), Silver Müller, etc.). These conditions on $\mathbf{E}$ and $\mathbf{H}$ only would be adequate for a local dispersion model where no bulk plasmons can appear. For the non-local dispersion this is not the case anymore and bulk plasmons can be excited [31]. This leads to the requirement of an additional boundary condition on $\mathbf{J}$. This is also justified by the fact that the equation determining the evolution of the polarization current in (9) is a PDE. As in our work the free electrons of a metal are described by a hydrodynamic model and quantum effects like tunneling are left out, it is physically reasonable to prohibit that electrons escape while they can freely move inside a metal. Motivated by this, we adopt as in Moreau et al. [8] the boundary condition

$$\mathbf{n} \cdot \mathbf{J}|_{\partial \Omega} = 0, \tag{12}$$

for the current density. This condition obtained by physical arguments is indeed compatible with the considered system of PDEs. The dual condition $Q = 0$ on the boundary of the non-local media may also be considered, and all the results presented in the following could easily be adapted. In the case of an interface between two different media e.g. one driven by a media that is not "non-local" (media 2) and another one driven by (9) (media 1), interface conditions will be applied. Classical interface conditions will hold for the Maxwell field. For the non-local current part the interface condition would read

$$\mathbf{n}_{12} \cdot (\mathbf{J}_2 - \mathbf{J}_1) = 0 \text{ with } \mathbf{J}_2 \equiv 0. \tag{13}$$

In the following theoretical results we consider $\Omega$ as an open bounded and convex domain.

## 2.5. Energy principle

An energy principle can be understood as a figure of merit of a physical model as the total energy stored in a physically motivated system must never increase. Additionally, preserving this property when it comes to numerical algorithms would be a nice feature of the latter. Formally defining the energy as

$$\mathcal{E} := \frac{1}{2} \left\{ \mu_0 \omega_p^2 \varepsilon_0 \|\mathbf{H}\|_{\mathcal{L}^2(\Omega)}^2 + \varepsilon_\infty \varepsilon_0^2 \omega_p^2 \|\mathbf{E}\|_{\mathcal{L}^2(\Omega)}^2 + \|\mathbf{J}\|_{\mathcal{L}^2(\Omega)}^2 + \beta^2 \|Q\|_{\mathcal{L}^2(\Omega)}^2 \right\}, \tag{14}$$

on the considered time interval, where $\mathcal{L}^2(\Omega)$ denotes the space of square integrable functions and $\|\cdot\|_{\mathcal{L}^2(\Omega)}$ its associated norm. Equation (14) together with (9) formally leads to

$$\partial_t \mathcal{E} = -\gamma \|\mathbf{J}\|_{\mathcal{L}^2(\Omega)}^2 \leq 0. \tag{15}$$

Here, where we have assumed that $\partial\Omega$ is a perfectly electric conducting boundary and that currents vanish outside $\Omega$, meaning that $\mathbf{E} \times \mathbf{n} = 0$ and $\mathbf{J} \cdot \mathbf{n} = 0$ on $\partial\Omega$ where $\mathbf{n}$ denotes the surface normal pointing outwards of $\partial\Omega$. The result obtained in (15) shows the strict preservation of the energy $\partial_t \mathcal{E}(t) = 0$ for a collision free model and does also drive dissipation if collisions (damping) are taken into account.

## 2.6. Mode splitting in the two-dimensional case

Considering a 2D computational domain in the $x, y$ plane being invariant in the $z$-direction, all derivatives with respect to $z$ vanish. Thus, as detailed in [33], the total solution of (8) can be separated into two independent sets of equations. Each set provides a solution where either the electric or magnetic field has only one spatial component and the corresponding magnetic or electric field is only polarized in the perpendicular plane, respectively. The system for the so-called TM mode has a $z$ polarized electrical field $\mathbf{E} = E_z \mathbf{e}_z$ with the corresponding transverse magnetic field $\mathbf{H} = H_x \mathbf{e}_x + H_y \mathbf{e}_y$, where $\mathbf{e}_u, u \in \{x, y, z\}$ are the cartesian basis vectors. Equally, the solution for TE mode shows a magnetic polarization in $z$ direction $\mathbf{H} = H_z \mathbf{e}_z$ with the corresponding transverse electric field $\mathbf{E} = E_x \mathbf{e}_x + E_y \mathbf{e}_y$. Easy calculations show the important fact that only the TE mode is able to excite a non-local polarization in the 2D case while the TM mode remains totally local. Thus, for the purpose of studying non-local effects in $\Omega$, it is sufficient to consider the system for the TE mode

$$\begin{aligned}
\partial_y H_z &= \varepsilon_0 \varepsilon_\infty \partial_t E_x + J_x + J_x, \\
-\partial_x H_z &= \varepsilon_0 \varepsilon_\infty \partial_t E_y + J_y + J_y, \\
\partial_x E_y - \partial_y E_x &= -\mu_0 \partial_t H_z, \\
\omega_p^2 \varepsilon_0 \partial_t E_x &= \partial_{tt} J_x + \gamma \partial_t J_x - \beta^2 (\partial_{xx} J_x + \partial_{xz} J_z), \\
\omega_p^2 \varepsilon_0 \partial_t E_y &= \partial_{tt} J_y + \gamma \partial_t J_y - \beta^2 (\partial_{yx} J_y + \partial_{yy} J_y).
\end{aligned} \tag{16}$$

## 2.7. Rescaling

We now want to rescale system (9) in order to simplify the equations and to focus on the quantities that change within space. Defining the vacuum impedance and speed of light $Z_0 = \sqrt{\frac{\mu_0}{\varepsilon_0}}$ and $c_0 = \frac{1}{\sqrt{\mu_0 \varepsilon_0}}$ and substituting the original quantities by

$$\left\{ \tilde{\mathbf{H}}, \tilde{\mathbf{E}}, \tilde{\mathbf{J}}, \tilde{Q}, \tilde{t}, \tilde{\beta}^2, \tilde{\gamma}, \tilde{\omega}_p \right\} := \left\{ Z_0 \mathbf{H}, \mathbf{E}, Z_0 \mathbf{J}, c_0 Z_0 Q, c_0 t, \frac{\beta^2}{c_0^2}, \frac{\gamma}{c_0}, \frac{\omega_p}{c_0} \right\}, \tag{17}$$

yields for system (9)

$$\begin{aligned}
\partial_{\tilde{t}} \tilde{\mathbf{H}} + \nabla \times \tilde{\mathbf{E}} &= 0, \\
\varepsilon_\infty \partial_{\tilde{t}} \tilde{\mathbf{E}} - \nabla \times \tilde{\mathbf{H}} &= -\tilde{\mathbf{J}}, \\
\partial_{\tilde{t}} \tilde{\mathbf{J}} - \tilde{\beta}^2 \nabla \tilde{Q} &= \tilde{\omega}_p^2 \tilde{\mathbf{E}} - \tilde{\gamma} \tilde{\mathbf{J}}, \\
\partial_{\tilde{t}} \tilde{Q} - \nabla \cdot \tilde{\mathbf{J}} &= 0.
\end{aligned} \tag{18}$$

This rescaled version of system (9) is not used in the following development of the DGTD scheme, but is has been adopted for the actual implementation.

## 3. The DGTD scheme

The previous section presented and discussed the physical framework we consider in this work. In this section we describe the spatial discretization based on a DG formulation. Since we work within a discontinuous framework, numerical fluxes have to be introduced. In this work, we only consider centered fluxes as a first approach. Further extensions to other fluxes are possible and will be part of a future work. The obtained semi-discrete system is then time integrated using an explicit scheme. A stability analysis is presented for both the semi-discrete and the fully-discrete scheme.

### 3.1. The discontinuous Galerkin method

The DG method was first proposed in the context of neutron transport problems by Reed and Hill in [44]. In the following years, the method has become very popular and has been applied to a vast field of computational physics and engineering topics. A very popular example is the field of computational fluid dynamics. Although most publications on DG are journal papers, the book of Hesthaven and Warburton [45] gives a comprehensive study of the DG method. Due to their local character, DG methods are very flexible in terms of *hp*-adaptivity and non-conformal grids. Additionally, the associated block diagonal mass matrix allows an efficient explicit time integration which would not be directly the case for continuous finite element method (FEM) in general. The discontinuity introduced in the approximation induces an increasing amount of discrete unknowns, which is an obvious drawback of the method. It can be overcome by exploiting the locality of the approach with a parallel implementation strategy. We now want to apply the DG method to system (9). This is done in the following steps. Defining a weak formulation, choosing an appropriate space for the basis functions and eventually evaluating the resulting integrals. Although the following derivations are done with scalar test functions (as used in the implementation), vectorial test functions are used for the subsequent stability analysis. Indeed, the equivalence of both formulations is guaranteed and this choice is only made for the sake of clarity.

### 3.2. Weak formulation

Let us derive the weak formulation of system (9) on which our discretization will be based. We denote by $H^1(\Omega)$ the space of square integrable functions with gradient in $\mathcal{L}^2(\Omega)$. We obtain $\forall \phi \in H^1(\Omega)^3$

$$
\begin{aligned}
\int_\Omega \mathbf{H} \times \nabla\phi \, \mathrm{d}^3\mathbf{r} + \int_{\partial\Omega} \phi(\mathbf{n} \times \mathbf{H}) \, \mathrm{d}^2\mathbf{r} &= \partial_t \int_\Omega \varepsilon_0\varepsilon_\infty\mathbf{E}\phi \, \mathrm{d}^3\mathbf{r} + \int_\Omega \mathbf{J}\phi \, \mathrm{d}^3\mathbf{r}, \\
\int_\Omega \mathbf{E} \times \nabla\phi \, \mathrm{d}^3\mathbf{r} + \int_{\partial\Omega} \phi(\mathbf{n} \times \mathbf{E}) \, \mathrm{d}^2\mathbf{r} &= -\partial_t \int_\Omega \mu_0\mathbf{H}\phi \, \mathrm{d}^3\mathbf{r}, \\
-\int_\Omega \beta^2 Q \nabla\phi \, \mathrm{d}^3\mathbf{r} + \int_{\partial\Omega} \beta^2\phi Q \mathbf{n} \, \mathrm{d}^2\mathbf{r} &= \partial_t \int_\Omega \mathbf{J}\phi \, \mathrm{d}^3\mathbf{r} + \int_\Omega \gamma\mathbf{J}\phi \, \mathrm{d}^3\mathbf{r} - \int_\Omega \varepsilon_0\omega_p^2\mathbf{E}\phi \, \mathrm{d}^3\mathbf{r}, \\
-\int_\Omega \mathbf{J} \cdot \nabla\phi \, \mathrm{d}^3\mathbf{r} + \int_{\partial\Omega} \phi\mathbf{J} \cdot \mathbf{n} \, \mathrm{d}^2\mathbf{r} &= \partial_t \int_\Omega Q\phi \, \mathrm{d}^3\mathbf{r}.
\end{aligned}
\tag{19}
$$

Spatial discretization with the DG method requires a special choice of polynomial basis functions. Unlike continuous FEM, the basis functions are local on each mesh element. In other words, each finite element, provides a set of basis functions that do not overlap with their neighbors. Due to the latter mentioned property, continuity of the fields is not enforced and discontinuities at the cell interfaces may arise. The treatment of those discontinuities provides an additional parameter for the design of the final algorithm. As we will see later, the discontinuities are important for the surface integrals in (19) and are handled by introducing a numerical flux. Depending on the chosen mesh topology, different polynomial basis expansions are possible. In our case, a tetrahedral mesh is assumed in combination with Lagrange polynomials. We thus suppose that the computational domain $\Omega$ can be discretized as a tetrahedral conformal and quasi-uniform mesh as $\overline{\Omega} = \bigcup_{\forall i \in \mathcal{N}_\Omega} \overline{\Omega}_i$, with $\mathcal{N}_\Omega$ being the set of indices of the mesh elements. We will denote the mesh size by $h > 0$. Furthermore, for all $i \in \mathcal{N}_\Omega$, $\mathcal{N}_{\Omega_i}$ will denote the set of indices of the neighboring elements of $\Omega_i$ (having a face in common) and $s_{iq} = \overline{\Omega}_i \cap \overline{\Omega}_q$, $\forall q \in \mathcal{N}_{\Omega_i}$, the set of internal faces. We will also classically denote by $h > 0$ the characteristic mesh parameter. We define the approximation space as

$$
\mathcal{V}^p(\Omega) := \left\{ v \in \mathcal{L}^2(\Omega), \, v|_{\Omega_i} \in \mathcal{P}_p(\Omega_i), \, \forall i \in \mathcal{N}_\Omega \right\},
\tag{20}
$$

where $\mathcal{P}_p(\Omega_i)$ is the space of polynomials of maximum degree $p \in \mathbb{N}$ on $\Omega_i$. $\mathcal{V}^p(\Omega)$ is a finite dimensional subspace of $\mathcal{L}^2(\Omega)$. We choose a polynomial basis of $\mathcal{V}^p(\Omega)$ formed by polynomial functions $(\phi_{ij})_{\mathcal{N}_\Omega \times [1,P_i]}$, with $P_i$ the number of Degrees of Freedom (DoFs) for the $i$-th element. For any $\mathbf{A} \in (\mathcal{V}^p)^3$, we denote by $\mathbf{A}_i$ the restriction of $\mathbf{A}$ to $\Omega_i$ (analogous definition holds for a scalar field of $\mathcal{V}^p$).

Let us describe the DG method: The discrete weak formulation is expressed locally on each element of the mesh. Then, one has to find $(\mathbf{E}, \mathbf{H}, Q, \mathbf{J}) \in (\mathcal{V}^p)^{10}$, such that for all for all $i \in \mathcal{N}_\Omega$, $k \in [\![0, P_i]\!]$

$$\int_{\Omega_i} \mathbf{H}_i \times \nabla\phi_{ik} \, \mathrm{d}^3\mathbf{r} + \int_{\partial\Omega_i} \phi_{ik}(\mathbf{n} \times \mathbf{H}_i^\star) \, \mathrm{d}^2\mathbf{r} = \partial_t \int_{\Omega_i} \varepsilon_0 \varepsilon_\infty \mathbf{E}_i \phi_{ik} \, \mathrm{d}^3\mathbf{r} + \int_{\Omega_i} \mathbf{J}_i \phi_{ik} \, \mathrm{d}^3\mathbf{r},$$

$$\int_{\Omega_i} \mathbf{E}_i \times \nabla\phi_{ik} \, \mathrm{d}^3\mathbf{r} + \int_{\partial\Omega_i} \phi_{ik}(\mathbf{n} \times \mathbf{E}_i^\star) \, \mathrm{d}^2\mathbf{r} = -\partial_t \int_{\Omega_i} \mu_0 \mathbf{H}_i \phi_{ik} \, \mathrm{d}^3\mathbf{r},$$

$$-\int_{\Omega_i} \beta^2 Q_i \nabla\phi_{ik} \, \mathrm{d}^3\mathbf{r} + \int_{\partial\Omega_i} \beta^2 \phi_{ik} Q_i^\star \mathbf{n} \, \mathrm{d}^2\mathbf{r} = \partial_t \int_{\Omega_i} \mathbf{J}_i \phi_{ik} \, \mathrm{d}^3\mathbf{r} + \int_{\Omega_i} \gamma \mathbf{J}_i \phi_{ik} \, \mathrm{d}^3\mathbf{r} - \int_{\Omega_i} \varepsilon_0 \omega_p^2 \mathbf{E}_i \phi_{ik} \, \mathrm{d}^3\mathbf{r},$$

$$-\int_{\Omega_i} \mathbf{J}_i \cdot \nabla\phi_{ik} \, \mathrm{d}^3\mathbf{r} + \int_{\partial\Omega_i} \phi_{ik}\mathbf{J}_i^\star \cdot \mathbf{n} \, \mathrm{d}^2\mathbf{r} = \partial_t \int_{\Omega_i} Q_i \phi_{ik} \, \mathrm{d}^3\mathbf{r}. \tag{21}$$

The additional $(\cdot)^\star$ emphasizes the field values on the boundary $\partial\Omega_i$ and will become clearer when the flux matrices are evaluated. We want to use this notation because of the field's discontinuity between two elements. Indeed, the field value at the interface is not well defined. Please note that, even though it is not emphasized on the notations (for the sake of clarity), all the discrete fields depend on $h$. The discrete field quantities can be expressed as

$$\mathbf{A}|_{\Omega_i}(t) = \mathbf{A}_i(t) := \sum_{u=1}^{3} \sum_{j=1}^{P_i} A_{ij}^u(t)\phi_{ij}\mathbf{e}_u, \quad \mathbf{A} \in \{\mathbf{H}, \mathbf{E}, \mathbf{J}\}, \tag{22a}$$

$$Q|_{\Omega_i}(t) = Q_i(t) := \sum_{j=1}^{P_i} Q_{ij}(t)\phi_{ij}, \tag{22b}$$

where $u \in \{1, 2, 3\}$ refers to the spatial variable. The expressions in (22) are polynomial approximations on each cell. Using these decompositions, the integral terms of (21) lead to the definition of elementary matrices on a reference element (used in the actual implementation). The *mass matrix* is deduced from integrals of the form $\int_{\Omega_i} \alpha \sum_{u=1}^{3} \sum_{j=1}^{P_i} A_{ij}^u \phi_{ij}\mathbf{e}_u \phi_{ik} \, \mathrm{d}^3\mathbf{r}$, where $\alpha$ is a generalized material parameter. Rewriting this expression in matrix form we define a vector containing the DoFs of the discrete fields by means of $\mathbf{A_i} \in \mathbb{R}^{3P_i}$ with $\{\mathbf{A_i}\}_{j+u \cdot P_i} = A_{ij}^u$, $j \in [\![1, P_i]\!]$. This allows to define

$$\left(\mathbb{M}_i^\alpha\right)_{kj}^u := \int_{\Omega_i} \alpha \phi_{ij}\phi_{ik} \, \mathrm{d}^3\mathbf{r}, \quad \mathbb{M}_i^\alpha = \mathrm{diag}\left\{\left(\mathbb{M}_i^\alpha\right)^1, \left(\mathbb{M}_i^\alpha\right)^2, \left(\mathbb{M}_i^\alpha\right)^3\right\}, \in \mathbb{R}^{3P_i \times 3P_i}. \tag{23}$$

In our case, we furthermore assume that the material parameters are piecewise constant per mesh element. Hence, (23) can be rewritten in the following form $\mathbb{M}_i = \alpha \, \mathrm{diag}\left\{(\mathbb{M}_i)^1, (\mathbb{M}_i)^2, (\mathbb{M}_i)^3\right\}, \in \mathbb{R}^{3P_i \times 3P_i}$. While the mass matrix does not involve any spatial derivatives, the *stiffness matrix* carries the *inner* part of the original differential operators' weak form. In other words, the spatial derivative is split into an *inner stiffness* and *outer flux* matrix. For the weak curl operator, the stiffness part reads

$$\int_{\Omega_i} \mathbf{A}_i \times \nabla\phi_{ik} \, \mathrm{d}^3\mathbf{r} = \int_{\Omega_i} \sum_{u=1}^{3} \sum_{j=1}^{P_i} A_{ij}^u \phi_{ij}\mathbf{e}_u \times \nabla\phi_{ik} \, \mathrm{d}^3\mathbf{r},$$

$$(\mathbb{S}_i)_{kj}^u := \int_{\Omega_i} \phi_{ij}\mathbf{e}_u \times \nabla\phi_{ik} \, \mathrm{d}^3\mathbf{r}, \quad \mathbb{S}_i = \mathrm{diag}\left\{(\mathbb{S}_i)^1, (\mathbb{S}_i)^2, (\mathbb{S}_i)^3\right\} \in \mathbb{R}^{3P_i \times 3P_i}.$$

Analogously for the grad term

$$\int_{\Omega_i} Q_i \nabla\phi_{ik} \, \mathrm{d}^3\mathbf{r} = \int_{\Omega_i} \sum_{j=1}^{P_i} Q_{ij}\phi_{ij}\nabla\phi_{ik} \, \mathrm{d}^3\mathbf{r} = \sum_{j=1}^{P_i} Q_{ij} \int_{\Omega_i} \phi_{ij}\nabla\phi_{ik} \, \mathrm{d}^3\mathbf{r},$$

$$(\mathbb{G}_i)_{kj}^u := \int_{\Omega_i} \phi_{ij}\partial_u\phi_{ik} \, \mathrm{d}^3\mathbf{r}, \quad \mathbb{G}_i := \begin{pmatrix} (\mathbb{G}_i)^1 \\ (\mathbb{G}_i)^2 \\ (\mathbb{G}_i)^3 \end{pmatrix} \in \mathbb{R}^{3P_i \times P_i},$$

with $\partial_1 = \partial_x$, $\partial_2 = \partial_y$, $\partial_3 = \partial_z$, and finally for the div term

$$\int_{\Omega_i} \mathbf{J}_i \cdot \nabla \phi_{ik} \, d^3\mathbf{r} = \int_{\Omega_i} \sum_{u=1}^{3} \sum_{j=1}^{P_i} J_{ij}^u \phi_{ij} \mathbf{e}_u \cdot \nabla \phi_{ik} \, d^3\mathbf{r} = \sum_{u=1}^{3} \sum_{j=1}^{P_i} J_{ij}^u \mathbf{e}_u \cdot \int_{\Omega_i} \phi_{ij} \nabla \phi_{ik} \, d^3\mathbf{r},$$

$$(\mathbb{D}_i)_{kj}^u := \int_{\Omega_i} \phi_{ij} \partial_u \phi_{ik} \, d^3\mathbf{r}, \quad \mathbb{D}_i := \left( (\mathbb{D}_i)^1 \quad (\mathbb{D}_i)^2 \quad (\mathbb{D}_i)^3 \right) \in \mathbb{R}^{P_i \times 3P_i}.$$

One of the special but also crucial points for the DG method is the definition of the field quantity at the boundary shared with neighboring cells. A centered numerical flux for example, usually have the advantage to exactly preserve the dissipative nature of the physical system without any artificial numerical dissipation. It averages the field quantities of the contributing elements at the cell interface $s_{iq}$ pointing from element $i$ to element $q$ according to $\mathbf{A}_i^\star = \dfrac{\mathbf{A}_i + \mathbf{A}_q}{2}$. Another possible approach is to use an upwind numerical flux analogously to finite volume schemes where the boundary value is defined with respect to wave propagation direction. This numerical flux induces artificial numerical dissipation while spurious solutions are damped in time and offer less numerical dispersion than a centered numerical fluxe. As a first attempt and first proof of principle, for the discretization of (9), we propose to focus on a centered scheme. It furthermore easily couples to leap-frog time scheme leading to a fully discrete scheme that preserves energy under certain conditions as shown in the following. The important case of upwind fluxes will be part of a future work towards a more comprehensive study of the full three dimensional problem (9).

We define the associated notation of the average of a field $\mathbf{A}$ on the interface between two neighboring elements $i$ and $q$ by means of $\{\mathbf{A}\}_{iq} := \dfrac{\mathbf{A}_i + \mathbf{A}_q}{2}\Big|_{s_{iq}}$. For Ampère's and Faraday's laws we obtain

$$\int_{\partial\Omega_i} \phi_{ik}(\mathbf{n} \times \mathbf{A}_i^\star) \, d^2\mathbf{r} = \sum_{q=1}^{N^i} \int_{s_{iq}} \phi_{ik}\left( \mathbf{n}_{iq} \times \frac{\mathbf{A}_i + \mathbf{A}_q}{2} \right) d^2\mathbf{r}$$

$$= \frac{1}{2} \sum_{q=1}^{N^i} \int_{s_{iq}} \left[ \underbrace{\phi_{ik}\left( \mathbf{n}_{iq} \times \mathbf{A}_i \right)}_{\text{self flux}} + \underbrace{\phi_{ik}\left( \mathbf{n}_{iq} \times \mathbf{A}_q \right)}_{\text{neighbor flux}} \right] d^2\mathbf{r}, \qquad (24)$$

where $N^i = \mathrm{card}(\mathcal{N}_{\Omega_i})$ is the number of neighbors of $\Omega_i$. Similarly as before, we derive the corresponding matrix of the self flux (superscript $s$) and of the neighbor flux (superscript $n$): for all $u \in \{1, 2, 3\}$, $i \in \mathcal{N}_\Omega$, $q \in [\![1, N^i]\!]$,

$$\left( (\mathbb{F}_{\mathrm{curl}})_{iq}^s \right)_{jk}^u = \int_{s_{iq}} \phi_{ik}\phi_{ij} \left( \mathbf{n}_{iq} \times \mathbf{e}_u \right) d^2\mathbf{r}, \quad \left( (\mathbb{F}_{\mathrm{curl}})_{iq}^n \right)_{jk}^u = \int_{s_{iq}} \phi_{ik}\phi_{qj} \left( \mathbf{n}_{iq} \times \mathbf{e}_u \right) d^2\mathbf{r}.$$

The boundary integral for $Q$ has a different structure and leads with the central flux to

$$\int_{\partial\Omega_i} \phi_{ik} Q_i^\star \mathbf{n} \, d^2\mathbf{r} = \sum_{q=1}^{N^i} \int_{s_{iq}} \phi_{ik} \left( \frac{Q_i + Q_q}{2} \right) \mathbf{n}_{iq} \, d^2\mathbf{r}. \qquad (25)$$

Continuing in the same manner as before yields

$$\left( (\mathbb{F}_{\mathrm{grad}})_{iq}^s \right)_{jk} = \int_{s_{iq}} \phi_{ik}\phi_{ij}\mathbf{n}_{iq} \, d^2\mathbf{r}, \quad \left( (\mathbb{F}_{\mathrm{grad}})_{iq}^n \right)_{jk} = \int_{s_{iq}} \phi_{ik}\phi_{qj}\mathbf{n}_{iq} \, d^2\mathbf{r},$$

for respectively the self and neighboring fluxes. Evaluating the flux terms for the polarization current leads to

$$\int_{\partial\Omega_i} \phi_{ik}\mathbf{J}_i^\star \cdot \mathbf{n} \, d^2\mathbf{r} = \sum_{q=1}^{N^i} \int_{s_{iq}} \phi_{ik} \left( \frac{\mathbf{J}_i + \mathbf{J}_q}{2} \right) \cdot \mathbf{n}_{iq} \, d^2\mathbf{r}. \qquad (26)$$

Hence, the corresponding matrices read

$$\left( (\mathbb{F}_{\mathrm{div}})_{iq}^s \right)_{jk}^u = \int_{s_{iq}} \phi_{ik}\phi_{ij}\mathbf{e}_u\mathbf{n}_{iq} \, d^2\mathbf{r}, \quad \left( (\mathbb{F}_{\mathrm{div}})_{iq}^n \right)_{jk}^u = \int_{s_{iq}} \phi_{ik}\phi_{qj}\mathbf{e}_u\mathbf{n}_{iq} \, d^2\mathbf{r}.$$

### 3.3. Semi-discrete stability

In order to study semi-discrete stability, we will exploit the weak formulation with vectorial test functions which reads $\forall i \in \mathcal{N}_\Omega$, $\forall (\phi_{i\mathbf{H}}, \phi_{i\mathbf{E}}, \phi_{i\mathbf{J}}, \phi_{iQ}) \in (\mathcal{V}^p)^{10}$,

$$\varepsilon_0 \varepsilon_\infty \partial_t \int_{\Omega_i} \mathbf{E}_i \cdot \phi_{i\mathbf{E}} \, \mathrm{d}^3\mathbf{r} = \int_{\Omega_i} \mathbf{H}_i \cdot (\nabla \times \phi_{i\mathbf{E}}) \, \mathrm{d}^3\mathbf{r} - \sum_{q=1}^{N^i} \int_{s_{iq}} \phi_{i\mathbf{E}} \cdot \left( \{\mathbf{H}\}_{iq} \times \mathbf{n}_{iq} \right) \, \mathrm{d}^2\mathbf{r} - \int_{\Omega_i} \mathbf{J}_i \cdot \phi_{i\mathbf{E}} \, \mathrm{d}^3\mathbf{r},$$

$$\mu_0 \partial_t \int_{\Omega_i} \mathbf{H}_i \cdot \phi_{i\mathbf{H}} \, \mathrm{d}^3\mathbf{r} = -\int_{\Omega_i} \mathbf{E}_i \cdot (\nabla \times \phi_{i\mathbf{H}}) \, \mathrm{d}^3\mathbf{r} + \sum_{q=1}^{N^i} \int_{s_{iq}} \phi_{i\mathbf{H}} \cdot \left( \{\mathbf{E}\}_{iq} \times \mathbf{n}_{iq} \right) \, \mathrm{d}^2\mathbf{r},$$

$$\partial_t \int_{\Omega_i} \mathbf{J}_i \cdot \phi_{i\mathbf{J}} \, \mathrm{d}^3\mathbf{r} = -\beta^2 \int_{\Omega_i} Q_i \nabla \cdot \phi_{i\mathbf{J}} \, \mathrm{d}^3\mathbf{r} + \beta^2 \sum_{q=1}^{N^i} \int_{s_{iq}} \{Q\}_{iq} \, \phi_{i\mathbf{J}} \cdot \mathbf{n}_{iq} \, \mathrm{d}^2\mathbf{r} + \omega_p^2 \varepsilon_0 \int_{\Omega_i} \mathbf{E}_i \cdot \phi_{i\mathbf{J}} \, \mathrm{d}^3\mathbf{r} - \gamma \int_{\Omega_i} \mathbf{J}_i \cdot \phi_{i\mathbf{J}} \, \mathrm{d}^3\mathbf{r},$$

$$\partial_t \int_{\Omega_i} Q_i \phi_{iQ} \, \mathrm{d}^3\mathbf{r} = -\int_{\Omega_i} \mathbf{J}_i \cdot \nabla \phi_{iQ} \, \mathrm{d}^3\mathbf{r} + \sum_{q=1}^{N^i} \int_{s_{iq}} \phi_{iQ} \, \{\mathbf{J}\}_{iq} \cdot \mathbf{n}_{iq} \, \mathrm{d}^2\mathbf{r}.$$

**Remark.** If $s_{iq}$ is a part of $\partial\Omega$, artificial elements can be used as described in [27]. We define the semi-discrete energy on each element $\Omega_i$ analogously to the analytical definition in (14) on the considered time interval

$$\mathcal{E}_i := \frac{1}{2} \left[ \mu_0 \omega_p^2 \varepsilon_0 \|\mathbf{H}_i\|_{\mathcal{L}^2(\Omega_i)}^2 + \varepsilon_\infty \varepsilon_0^2 \omega_p^2 \|\mathbf{E}_i\|_{\mathcal{L}^2(\Omega_i)}^2 + \|\mathbf{J}_i\|_{\mathcal{L}^2(\Omega_i)}^2 + \beta^2 \|Q_i\|_{\mathcal{L}^2(\Omega_i)}^2 \right].$$

The total energy is thus defined as

$$\mathcal{E}(t) = \sum_{i \in \mathcal{N}_\Omega} \mathcal{E}_i(t). \tag{27}$$

Differentiating formally in time, we find using the above weak formulation with the appropriate test functions

$$\partial_t \mathcal{E}_i = \omega_p^2 \varepsilon_0 \sum_{q=1}^{N^i} \int_{s_{iq}} \left[ \mathbf{H}_i \cdot \left( \{\mathbf{E}\}_{iq} \times \mathbf{n}_{iq} \right) - \mathbf{E}_i \cdot \left( \{\mathbf{H}\}_{iq} \times \mathbf{n}_{iq} \right) \right] \, \mathrm{d}^2\mathbf{r}$$

$$+ \omega_p^2 \varepsilon_0 \int_{\Omega_i} \left[ \mathbf{E}_i \cdot (\nabla \times \mathbf{H}_i) - \mathbf{H}_i \cdot (\nabla \times \mathbf{E}_i) \right] \, \mathrm{d}^3\mathbf{r}$$

$$+ \beta^2 \sum_{q=1}^{N^i} \left( \{Q\}_{iq} \mathbf{J}_i \cdot \mathbf{n}_{iq} + Q_i \{\mathbf{J}\}_{iq} \cdot \mathbf{n}_{iq} \right) \, \mathrm{d}^2\mathbf{r}$$

$$- \beta^2 \int_{\Omega_i} \nabla \cdot (Q_i \mathbf{J}_i) \, \mathrm{d}^3\mathbf{r} - \gamma \|\mathbf{J}_i\|_{\mathcal{L}^2(\Omega_i)}^2.$$

Integration by parts of one half of $\mathbf{E}_i \cdot (\nabla \times \mathbf{H}_i)$ and $\mathbf{H}_i \cdot (\nabla \times \mathbf{E}_i)$, respectively, and applying Gauss' theorem to the last integral of the div term yields

$$\partial_t \mathcal{E}_i = \frac{1}{2} \omega_p^2 \varepsilon_0 \sum_{q=1}^{N^i} \int_{s_{iq}} \left[ \mathbf{H}_i \cdot \left( \mathbf{E}_q \times \mathbf{n}_{iq} \right) - \mathbf{E}_i \cdot \left( \mathbf{H}_q \times \mathbf{n}_{iq} \right) \right] \, \mathrm{d}^2\mathbf{r}$$

$$+ \beta^2 \sum_{q=1}^{N^i} \int_{s_{iq}} \left( Q_q \mathbf{J}_i \cdot \mathbf{n}_{iq} + Q_i \mathbf{J}_q \cdot \mathbf{n}_{iq} \right) \, \mathrm{d}^2\mathbf{r} - \gamma \|\mathbf{J}_i\|_{\mathcal{L}^2(\Omega_i)}^2. \tag{28}$$

Summing over all elements $i$ and assuming metallic boundary conditions $\mathbf{E} \times \mathbf{n} = 0$ and $\mathbf{J} \cdot \mathbf{n} = 0$ on $\partial\Omega$, we obtain

$$\partial_t \mathcal{E} = -\gamma \|\mathbf{J}\|_{\mathcal{L}^2(\Omega_i)}^2. \tag{29}$$

Thus, the semi-discrete stability is guaranteed and a decrease of the energy is observed for lossy media.[3]

### 3.4. Time discretization with the leap-frog scheme

The DG method is used for the spatial discretization and leads to the system of ODEs (21) that one has to time integrate. In our case, we will introduce a staggered time grid where the electric field as well as the charge density are allocated on the primary grid and the magnetic field as well as the current density on the dual grid, respectively. We consider the problem on the time interval $[\![0, T]\!]$, with $T > 0$ and discretize the latter by a uniform subdivision $(t_n)_{n \in [\![0,N]\!]}$, $N \in \mathbb{N}^*$ of size $\Delta t$. The dual grid is shifted in time by $\frac{\Delta t}{2}$ with respect to the primary one. This approach was first proposed in the context of the FDTD method for Maxwell's equations in [46] and is also known as leap-frog scheme. Applying a second order leap-frog scheme to system (21) and using again vectorial test functions as in subsection 3.3, we obtain the following fully discrete scheme: for $n \in [\![0, N]\!]$, find $(\mathbf{E}^n, \mathbf{H}^{n+\frac{1}{2}}, \mathbf{J}^{n+\frac{1}{2}}, Q^n) \in (\mathcal{V}^p)^{10}$ such that $\forall i \in \mathcal{N}_\Omega$, $\forall (\phi_{i\mathbf{H}}, \phi_{i\mathbf{E}}, \phi_{i\mathbf{J}}, \phi_{iQ}) \in (\mathcal{V}^p)^{10}$,

$$
\varepsilon_0 \varepsilon_\infty \int_{\Omega_i} \frac{\mathbf{E}_i^{n+1} - \mathbf{E}_i^n}{\Delta t} \cdot \phi_{i\mathbf{E}} = \int_{\Omega_i} \mathbf{H}_i^{n+\frac{1}{2}} \cdot (\nabla \times \phi_{i\mathbf{E}})
$$
$$
- \sum_{q=1}^{N^i} \int_{s_{iq}} \phi_{i\mathbf{E}} \cdot \left( \left\{ \mathbf{H}^{n+\frac{1}{2}} \right\}_{iq} \times \mathbf{n}_{iq} \right) - \int_{\Omega_i} \mathbf{J}_i^{n+\frac{1}{2}} \cdot \phi_{i\mathbf{E}},
$$
(30a)

$$
\mu_0 \int_{\Omega_i} \frac{\mathbf{H}_i^{n+\frac{3}{2}} - \mathbf{H}_i^{n+\frac{1}{2}}}{\Delta t} \cdot \phi_{i\mathbf{H}} = -\int_{\Omega_i} \mathbf{E}_i^{n+1} \cdot (\nabla \times \phi_{i\mathbf{H}})
$$
$$
+ \sum_{q=1}^{N^i} \int_{s_{iq}} \phi_{i\mathbf{H}} \cdot \left( \left\{ \mathbf{E}^{n+1} \right\}_{iq} \times \mathbf{n}_{iq} \right),
$$
(30b)

$$
\int_{\Omega_i} \frac{\mathbf{J}_i^{n+\frac{3}{2}} - \mathbf{J}_i^{n+\frac{1}{2}}}{\Delta t} \cdot \phi_{i\mathbf{J}} = -\beta^2 \int_{\Omega_i} Q_i^{n+1} \nabla \cdot \phi_{i\mathbf{J}} + \beta^2 \sum_{q=1}^{N^i} \int_{s_{iq}} \left\{ Q^{n+1} \right\}_{iq} \phi_{i\mathbf{J}} \cdot \mathbf{n}_{iq}
$$
$$
+ \omega_p^2 \varepsilon_0 \int_{\Omega_i} \mathbf{E}_i^{n+1} \cdot \phi_{i\mathbf{J}} - \gamma \int_{\Omega_i} \frac{\mathbf{J}_i^{n+\frac{3}{2}} + \mathbf{J}_i^{n+\frac{1}{2}}}{2} \cdot \phi_{i\mathbf{J}},
$$
(30c)

$$
\int_{\Omega_i} \frac{Q_i^{n+1} - Q_i^n}{\Delta t} \phi_{iQ} = -\int_{\Omega_i} \mathbf{J}_i^{n+\frac{1}{2}} \cdot \nabla \phi_{iQ} + \sum_{q=1}^{N^i} \int_{s_{iq}} \phi_{iQ} \left\{ \mathbf{J}^{n+\frac{1}{2}} \right\}_{iq} \cdot \mathbf{n}_{iq}.
$$
(30d)

Taking this fully-discrete scheme as a starting point, we now study its stability.

### 3.5. Variation of the fully-discrete energy

We study here the evolution in discrete time of a fully discrete energy. We will proceed in a similar way as in the semi-discrete case. We first define $\mathcal{E}_i^{n+\frac{1}{2}}$ with some arbitrary coefficients for the energy norm by means of

$$
\mathcal{E}_i^{n+\frac{1}{2}} := \frac{1}{2} \left[ a \int_{\Omega_i} \mathbf{H}_i^{n+\frac{1}{2}} \cdot \mathbf{H}_i^{n+\frac{1}{2}} + b \int_{\Omega_i} \mathbf{E}_i^{n+1} \cdot \mathbf{E}_i^n + c \int_{\Omega_i} \mathbf{J}_i^{n+\frac{1}{2}} \cdot \mathbf{J}_i^{n+\frac{1}{2}} + d \int_{\Omega_i} Q_i^{n+1} \cdot Q_i^n \right].
$$
(31)

The introduced coefficients $(a, b, c, d) \in \mathbb{R}^4$ will be adapted later in order to obtain the decrease of the discrete energy[4] $\mathcal{E}^{n+\frac{1}{2}} = \sum_i \mathcal{E}_i^{n+\frac{1}{2}}$.

---

[3]  The term lossy refers here to the friction of electrons due to $\gamma$.

[4]  We have let the coefficients $(a, b, c, d)$ as degrees of freedom, since we found interesting to show which choice would make the fully discrete energy decrease.

Let us define an artificial time level for quantities allocated on the dual time grid e.g. $\mathbf{H}_i^{n+\frac{1}{2}}$ and $\mathbf{H}_i^{n+\frac{3}{2}}$, as $\mathbf{A}_i^{[n+1]} := \frac{\mathbf{A}_i^{n+\frac{3}{2}} + \mathbf{A}_i^{n+\frac{1}{2}}}{2}$. Using this definition together with the energy defined in (31), the energy difference between time step $n+\frac{3}{2}$ and $n+\frac{1}{2}$, denoted by $\Delta \mathcal{E}_i^{n+1} = \mathcal{E}_i^{n+\frac{3}{2}} - \mathcal{E}_i^{n+\frac{1}{2}}$, reads

$$2\Delta\mathcal{E}_i^{n+1} = 2a \int_{\Omega_i} \left( \mathbf{H}_i^{n+\frac{3}{2}} - \mathbf{H}_i^{n+\frac{1}{2}} \right) \cdot \mathbf{H}_i^{[n+1]} + b \int_{\Omega_i} \left( \mathbf{E}_i^{n+2} \cdot \mathbf{E}_i^{n+1} - \mathbf{E}_i^{n+1} \cdot \mathbf{E}_i^n \right)$$
$$+ 2c \int_{\Omega_i} \left( \mathbf{J}_i^{n+\frac{3}{2}} - \mathbf{J}_i^{n+\frac{1}{2}} \right) \cdot \mathbf{J}_i^{[n+1]} + d \int_{\Omega_i} \left( Q_i^{n+2} Q_i^{n+1} - Q_i^{n+1} Q_i^n \right). \tag{32}$$

We then make an appropriate choice of the test functions at the time level $t_{n+1}$ and use the equations of (30) at the time levels $t_{n+1}, t_{n+\frac{1}{2}}$ and $t_{n+\frac{3}{2}}$ according to (30a) at time $t_{n+\frac{1}{2}}$ and $t_{n+\frac{3}{2}}$ with $\mathbf{E}_i^{n+1}$, (30b) at time $t_{n+1}$ with $\mathbf{H}_i^{[n+1]}$, (30c) at time $t_{n+1}$ with $\mathbf{J}_i^{[n+1]}$, and (30d) at time $t_{n+\frac{1}{2}}$ and $t_{n+\frac{3}{2}}$ with $Q_i^{n+1}$; (32) can then be written as

$$\Delta\mathcal{E}_i^{n+1} = \int_{\Omega_i} \left[ b\frac{\Delta t}{\varepsilon_0 \varepsilon_\infty} \mathbf{H}_i^{[n+1]} \cdot \left( \nabla \times \mathbf{E}_i^{n+1} \right) - a\frac{\Delta t}{\mu_0} \mathbf{E}_i^{n+1} \cdot \left( \nabla \times \mathbf{H}_i^{[n+1]} \right) \right]$$
$$+ \sum_{q \in V_i} \int_{S_{iq}} \left[ a\frac{\Delta t}{\mu_0} \mathbf{H}_i^{[n+1]} \cdot \left( \left\{ \mathbf{E}^{n+1} \right\}_{iq} \times \mathbf{n}_{iq} \right) - b\frac{\Delta t}{\varepsilon_0 \varepsilon_\infty} \mathbf{E}_i^{n+1} \cdot \left( \left\{ \mathbf{H}^{[n+1]} \right\}_{iq} \times \mathbf{n}_{iq} \right) \right]$$
$$- \int_{\Omega_i} \left[ c\Delta t\beta^2 Q_i^{n+1} \nabla \cdot \mathbf{J}_i^{[n+1]} + d\Delta t\mathbf{J}_i^{[n+1]} \cdot \nabla Q_i^{n+1} \right]$$
$$+ \Delta t \sum_{q \in V_i} \int_{S_{iq}} \left[ c\beta^2 \left\{ Q^{n+1} \right\}_{iq} \mathbf{J}_i^{[n+1]} \cdot \mathbf{n}_{iq} + d\, Q_i^{n+1} \left\{ J^{n+1} \right\}_{iq} \cdot \mathbf{n}_{iq} \right]$$
$$- b\frac{\Delta t}{\varepsilon_0 \varepsilon_\infty} \int_{\Omega_i} \mathbf{J}_i^{[n+1]} \cdot \mathbf{E}_i^{n+1} + c\omega_p^2 \varepsilon_0 \Delta t \int_{\Omega_i} \mathbf{E}_i^{n+1} \cdot \mathbf{J}_i^{[n+1]} - c\gamma\Delta t \int_{\Omega_i} \mathbf{J}_i^{[n+1]} \cdot \mathbf{J}_i^{[n+1]}.$$

Here, the set $V_i$ denotes all interfaces of element $i$ by means of $V_i = V_i^{int} \cup V_i^{ext}$ ($\overline{V}_i^{int} \cap \overline{V}_i^{ext} = \emptyset$) where $V_i^{int}$ contains the inner interfaces and $V_i^{ext}$ the interfaces that intersect with the boundary of the computational domain $\Omega$. Integrating by parts and setting $d = c\beta^2$ and $b = a\frac{\varepsilon_0 \varepsilon_\infty}{\mu_0}$ finally leads to

$$\Delta\mathcal{E}_i^{n+1} = a\frac{\Delta t}{\mu_0} \sum_{q \in V_i} \int_{S_{iq}} \left[ \mathbf{H}_i^{[n+1]} \cdot \left( \frac{\mathbf{E}_q^{n+1}}{2} \times \mathbf{n}_{iq} \right) - \mathbf{E}_i^{n+1} \cdot \left( \frac{\mathbf{H}_q^{[n+1]}}{2} \times \mathbf{n}_{iq} \right) \right]$$
$$+ c\beta^2 \Delta t \sum_{q \in V_i} \int_{S_{iq}} \left( Q_q^{n+1} \mathbf{J}_i^{[n+1]} \cdot \mathbf{n}_{iq} + Q_i^{n+1} \mathbf{J}_q^{[n+1]} \cdot \mathbf{n}_{iq} \right)$$
$$- a\frac{\Delta t}{\mu_0} \int_{\Omega_i} \mathbf{J}_i^{[n+1]} \cdot \mathbf{E}_i^{n+1} + c\omega_p^2 \varepsilon_0 \Delta t \int_{\Omega_i} \mathbf{E}_i^{n+1} \cdot \mathbf{J}_i^{[n+1]} - c\gamma\Delta t \int_{\Omega_i} \mathbf{J}_i^{[n+1]} \cdot \mathbf{J}_i^{[n+1]}.$$

Choosing the relation between $a$ and $c$ appropriately as $a = c\mu_0\omega_p^2\varepsilon_0$ and summing over all cells gives the total energy difference

$$\mathcal{E}^{n+\frac{3}{2}} - \mathcal{E}^{n+\frac{1}{2}} \leq -\gamma\Delta t \|\mathbf{J}^{[n+1]}\|_{\mathcal{L}^2(\Omega)}^2. \tag{33}$$

This is indeed a remarkable result because the purely centered DG scheme does not unphysically increase the energy for the coupled problem of Maxwell *together* with the non-local dispersion model. Additionally, the scheme is energy preserving if electron collisions are neglected.

### 3.6. Positivity of the fully-discrete energy

We now want to study the positivity of the fully-discrete energy with the adequate choice for the coefficients as defined in 3.5. Thus for each element $i \in \mathcal{N}_\Omega$,

$$\mathcal{E}_i^{n+\frac{1}{2}} := \frac{1}{2}\mu_0\omega_p^2\varepsilon_0\|\mathbf{H}_i^{n+\frac{1}{2}}\|_{\mathcal{L}^2(\Omega_i)}^2 + \frac{1}{2}\varepsilon_\infty\varepsilon_0^2\omega_p^2\int_{\Omega_i}\mathbf{E}_i^{n+1}\cdot\mathbf{E}_i^n + \frac{1}{2}\|\mathbf{J}_i^{n+\frac{1}{2}}\|_{\mathcal{L}^2(\Omega_i)}^2 + \frac{1}{2}\beta^2\int_{\Omega_i}Q_i^{n+1}\cdot Q_i^n. \tag{34}$$

This energy may not be positive due to the terms $\int_{\Omega_i}\mathbf{E}_i^{n+1}\cdot\mathbf{E}_i^n$ and $\frac{1}{2}\beta^2\int_{\Omega_i}Q_i^{n+1}\cdot Q_i^n$. However, testing (30a) and (30d) with $\mathbf{E}_i^n$ and $Q_i^n$, respectively, gives

$$\int_{\Omega_i}\mathbf{E}_i^{n+1}\cdot\mathbf{E}_i^n = \frac{\Delta t}{\varepsilon_0\varepsilon_\infty}\left[\int_{\Omega_i}\mathbf{H}_i^{n+\frac{1}{2}}\cdot(\nabla\times\mathbf{E}_i^n) - \sum_{q=1}^{N^i}\int_{s_{iq}}\mathbf{E}_i^n\cdot\left(\left\{\mathbf{H}^{n+\frac{1}{2}}\right\}_{iq}\times\mathbf{n}_{iq}\right) - \int_{\Omega_i}\mathbf{J}_i^{n+\frac{1}{2}}\cdot\mathbf{E}_i^n\right] + \|\mathbf{E}_i^n\|_{\Omega_i}^2,$$

$$\int_{\Omega_i}Q_i^{n+1}Q_i^n = \Delta t\left[-\int_{\Omega_i}\mathbf{J}_i^{n+\frac{1}{2}}\cdot\nabla Q_i^n + \sum_{q=1}^{N^i}\int_{s_{iq}}Q_i^n\left\{\mathbf{J}^{n+\frac{1}{2}}\right\}_{iq}\cdot\mathbf{n}_{iq}\right] + \|Q_i^n\|_{\mathcal{L}^2(\Omega_i)}^2.$$

We now plug these two expressions into (34). Using classical inverse inequalities [47] together with appropriate Cauchy–Schwarz inequalities, it can be shown that (we refer to [33] for more details) there exists a positive constant $C$, independent of $\Delta t$ and $h$, such that $\forall i\in\mathcal{N}_\Omega$

$$\begin{aligned}
\mathcal{E}_i^{n+\frac{1}{2}} \geq{}& \|\mathbf{H}_i\|_{\mathcal{L}^2(\Omega_i)}^2 + \varepsilon_\infty\varepsilon_0^2\omega_p^2\|\mathbf{E}_i\|_{\mathcal{L}^2(\Omega_i)}^2 + \|\mathbf{J}_i\|_{\mathcal{L}^2(\Omega_i)}^2 + \beta^2\|Q_i\|_{\mathcal{L}^2(\Omega_i)}^2 \\
&- \frac{\Delta t C\varepsilon_0\omega_p^2}{4h}\left[\|\mathbf{E}_i\|_{\mathcal{L}^2(\Omega_i)}^2 + \|\mathbf{H}_i\|_{\mathcal{L}^2(\Omega_i)}^2 + \sum_{q\in V_i^{int}}\left(\|\mathbf{E}_i\|_{\mathcal{L}^2(\Omega_i)}^2 + \|\mathbf{H}_q\|_{\mathcal{L}^2(\Omega_q)}^2\right)\right. \\
&+ \sum_{q\in V_i^{ext}}\left(\|\mathbf{E}_i\|_{\mathcal{L}^2(\Omega_i)}^2 + \|\mathbf{H}_i\|_{\mathcal{L}^2(\Omega_i)}^2\right) + \frac{2h}{C}\left(\|\mathbf{E}_i\|_{\mathcal{L}^2(\Omega_i)}^2 + \|\mathbf{J}_i\|_{\mathcal{L}^2(\Omega_i)}^2\right)\bigg] \\
&- \frac{\Delta t C\beta^2}{4h}\left[\|\mathbf{J}_i\|_{\mathcal{L}^2(\Omega_i)}^2 + \|Q\|_{\mathcal{L}^2(\Omega_i)}^2 + \sum_{q\in V_i^{int}}\left(\|Q_i\|_{\mathcal{L}^2(\Omega_i)}^2 + \|\mathbf{J}_q\|_{\mathcal{L}^2(\Omega_q)}^2\right) +\right. \\
&+ \sum_{q\in V_i^{ext}}\left(\|Q_i\|_{\mathcal{L}^2(\Omega_i)}^2 + \|\mathbf{J}_i\|_{\mathcal{L}^2(\Omega_i)}^2\right)\bigg],
\end{aligned}$$

where the superscripts for the time level have been omitted for the quantities in the right-hand side to ease the reading. Summing over all cells and adjusting $C$ yields

$$\begin{aligned}
\mathcal{E}^{n+\frac{1}{2}} \geq{}& \left[1 - \frac{C\Delta t\varepsilon_0\omega_p^2}{h}\left(2 + \frac{1}{4}\right)\right]\|\mathbf{H}\|_{\mathcal{L}^2(\Omega)}^2 \\
&+ \left[\varepsilon_\infty\varepsilon_0^2\omega_p^2 - \frac{1}{2}\Delta t\varepsilon_0\omega_p^2 - \frac{C\Delta t\varepsilon_0\omega_p^2}{h}\left(2 + \frac{1}{4}\right)\right]\|\mathbf{E}\|_{\mathcal{L}^2(\Omega)}^2 \\
&+ \left[1 - \frac{1}{2}\Delta t\varepsilon_0\omega_p^2 - \frac{C\Delta t\beta^2}{h}\left(2 + \frac{1}{4}\right)\right]\|\mathbf{J}\|_{\mathcal{L}^2(\Omega)}^2 \\
&+ \left[1 - \frac{C\Delta t}{h}\left(2 + \frac{1}{4}\right)\right]\|Q\|_{\mathcal{L}^2(\Omega)}^2. \tag{35}
\end{aligned}$$

Thus, the discrete energy will be positive definite if all the coefficients in front of the $\|\cdot\|_\Omega$ terms are positive. Inspired by this argument, we introduce a stability criterion for the time step $\Delta t$ in the time stepping scheme proposed above.

**Proposition 1** (*Positivity of the energy*). *The energy defined by (34) is positive under the following condition*

$$\frac{\Delta t}{4h} \leq \min\left\{\frac{1}{9\omega_p^2\varepsilon_0 C}, \frac{\varepsilon_0\varepsilon_\infty}{2h + 9C}, \frac{1}{2h\varepsilon_0\omega_p^2 + 9\beta^2 C}, \frac{1}{9C}\right\}, \tag{36}$$

*where $C$ is a generic constant independent of $\Delta t$ and $h$.*

Proposition 1 is commonly known as a CFL type criterion.

**Table 1**
Simulation parameters for the artificial test cavity. Here, $a$ denotes the length of the cubic domain $\Omega_\square$, $h$ the mesh size, $f$ the frequency of the $TE_{1,1}$ mode, and $\lambda$ the corresponding wavelength.

| $a$/nm | $h$/nm | $f$/PHz | $\lambda$/nm |
|---|---|---|---|
| 10 | 0.1, 0.05, 0.025, 0.0125, 0.008$\overline{3}$ | 21.21 | 14.1 |

## 4. Numerical results

We now discuss the numerical evaluation of the DGTD scheme presented in the previous sections. We first consider an artificial test case in order to validate the computer implementation of the numerical scheme (30), and then present results for a more classical problem relevant to nanoplasmonics.

### 4.1. Implementation

The DGTD method for the non-local dispersion model presented previously has been implemented in a 2D setting for the TE Maxwell's equations. From now on, we will use the notation DGTD-$\mathcal{P}_p$[5] when using polynomial interpolation of degree $p \in \mathbb{N}$. Due to the second order accuracy of the leap-frog time integration scheme, numerical simulations have been limited to $p \leq 2$. All routines were implemented in Fortran without putting a special effort into performance aspects. Especially, the implementation does not provide any parallelization.[6] Several test cases have been used in the scope of this work (see [33] for more details). As a test of the spatial discretization and the functionality of the algorithm, we want to compute the field solutions in a cavity that is artificially filled with dispersive metal. After having verified the algorithm's functionality, we stepped further to a more applied and physical test case.

### 4.2. Dispersive cavity

As a first test case, we consider a cavity which is completely filled with dispersive material. Although this is a rather unrealistic test case, it is a simple possibility to test the basic functionalities of the implementation. Our test case is inspired by [24] and combines the analytical solutions of the electromagnetic and hydrodynamic quantities of a vacuum filled and fully-dispersive cavity, respectively. In order to compensate the actual coupling of both equations, an artificial test current density is introduced. The construction of the latter is based on the analytical solution of the homogeneous Maxwell's equations coupled with the non-local dispersion model on a square domain $\Omega_\square = \{(x, y) \in [0, a] \times [0, a]\}$ for $a > 0$ given, with the PEC boundary condition

$$\mathbf{n}_{\Omega_\square} \times \mathbf{E} = 0 \text{ on } \in \partial\Omega_\square \times \mathbb{R}^+, \tag{37}$$

and

$$\mathbf{n}_{\Omega_\square} \cdot \mathbf{J} = 0, \text{ on } \in \partial\Omega_\square \times \mathbb{R}^+, \tag{38}$$

namely the eigenmodes in a cavity. The resulting formulation of the test case then reads

$$\nabla \times \mathbf{E} + \mu_0 \partial_t \mathbf{H} = 0, \tag{39a}$$

$$\nabla \times \mathbf{H} - \varepsilon_0 \partial_t \mathbf{E} = \mathbf{J} - \mathbf{J}^{art}, \tag{39b}$$

$$\beta^2 \nabla Q - \partial_t \mathbf{J} = \gamma_c \mathbf{J} - \varepsilon_0 \omega_p^2 \mathbf{E} - \tilde{\mathbf{J}}^{art}, \tag{39c}$$

$$\nabla \cdot \mathbf{J} - \partial_t Q = 0. \tag{39d}$$

$\mathbf{J}^{art}$ and $\tilde{\mathbf{J}}^{art}$ are the artificial currents that have been artificially introduced so that we can derive an exact solution denoted as $(\mathbf{E}^{exa}, \mathbf{H}^{exa}, \mathbf{J}^{exa}, Q^{exa})$. As the actual computational results for this test case are rather unphysical, we focus on the convergence behavior of the algorithm. Defining an error norm $\|\mathbf{E} - \mathbf{E}^a\|^2_{\mathcal{L}^2(\Omega)}$ on the domain $\Omega$ by $\|\mathbf{E} - \mathbf{E}^a\|^2_{\mathcal{L}^2(\Omega)} := \sum_{i \in \mathcal{N}_\Omega} \|\mathbf{E}_i - \mathbf{E}^{exa}\|^2_{\mathcal{L}^2(\Omega_i)}$ allows the evaluation of an error between the numerically computed and analytical solution. Fig. 1 illustrates the convergence behavior for the runs corresponding to Table 1. These results show that we obtain a numerical convergence of order 1 for the DGTD-$\mathcal{P}_1$ scheme and of order 2 for the DGTD-$\mathcal{P}_2$ scheme, which corresponds to usual convergence rates obtained for DGTD schemes based on a centered flux.

---

[5] We consider the same interpolation degree $p$ on each cell of the mesh.
[6] For this first study in 2D, this is not a concern. This will be however the case in 3D and will be the subject of a future work.
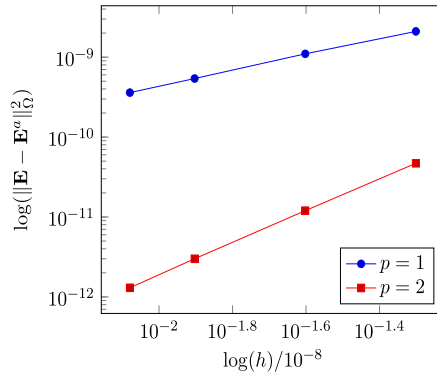
**Fig. 1.** $\mathcal{L}^2(\Omega)$-error for DGTD-$\mathcal{P}_1$ and DGTD-$\mathcal{P}_2$. The convergence rate is 1 and 2 for DGTD-$\mathcal{P}_1$ and DGTD-$\mathcal{P}_2$, respectively. Higher polynomial grades are not reasonable since a second order time integration scheme is used. The convergence order can be obtained by $p = \frac{\log(h_2)/\log(h_1)}{\log(\|\mathbf{E}-\mathbf{E}^a\|_\Omega^{h_1})/\log(\|\mathbf{E}-\mathbf{E}^a\|_\Omega^{h_2})}$. Here, $h_1$ and $h_2$ are two values for $h$ with $h_2 \neq h_1$.
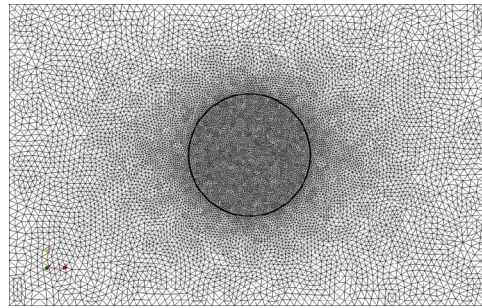


**Fig. 2.** Triangular mesh for a 2 nm dispersive nano disk. The dispersive regime requires a very strong refinement with respect to the usual mesh size for Maxwell's equations. This is mainly caused by the comparatively short wavelength of the bulk plasmon.

### 4.3. Nanodisk

In order to consider a more physical configuration and to demonstrate the impact of non-local dispersion effects, we simulate the scattering of a plane wave by an infinitely long wire, i.e. a nanodisk. We have chosen this example in order to compare our results in the time domain with the solutions given in [31] (and thus by extension, to [29]). In a first step, a numerical discussion on accuracy and computational time with respect to the interpolation degree $p$ is given. Physical aspects like the excitation of surface and bulk plasmons are discussed afterwards. In order to guarantee the same experimental setup, we have taken the physical parameters and excitation frequencies from [31] that are summarized in Table 3. A sinusoidal modulated gaussian pulse is used for illumination by means of a plane wave. The temporal modulation is determined by an incident TE wave that is linearly polarized in $x$ and $z$ direction for $\mathbf{E}$ and $\mathbf{H}$, respectively as

$$\{\mathbf{E}_{inc}(t), \mathbf{H}_{inc}(t)\} \propto \sin(\omega_c(t - \tau)) \exp\left(-\left(\frac{t - \tau}{\alpha}\right)^2\right). \tag{40}$$

The illumination is consequently oriented in $-\mathbf{e}_y$. Table 4 summarizes the chosen parameters for the excitation signal for the runs with $\omega_c$ below and above the plasma frequency. Fig. 2 shows the triangular mesh used in the simulations. It is very important to provide a sufficiently small mesh size in the dispersive region due to the small wavelength of the bulk plasmons. On the boundary of the domain, we apply an absorbing boundary condition and the incident field is orthogonally induced from above. For switching from the local to the non-local model, the parameter $\beta$ is set from 0 to the value given in Table 3. The relative permittivity $\varepsilon_\infty$ is set to 1 everywhere. Details on the computational parameters are summarized in Table 2.

Let us discuss numerical aspects of the implemented DGTD-$\mathcal{P}_p$ method with $p \in \{1, 2\}$. Within this work we limit those aspects to visual effects that can be seen in a 2D plot of the computed fields. As a figure of merit, we use the absolute value of the discrete Fourier transform of the computed field quantities. Visualizing the transformed fields at the frequencies $\omega_{c,1}$ and $\omega_{c,2}$ allows a comparison with frequency domain solutions. Fig. 3 shows the results for $\mathcal{P}_1$ and $\mathcal{P}_2$ interpolation polynomials. Our solutions show a good visual agreement with the mode patterns published in [31] for the DGTD-$\mathcal{P}_2$ run while the solution for DGTD-$\mathcal{P}_1$ is rather blurry. A mesh refinement would improve the quality of the DGTD-$\mathcal{P}_1$ solution. A computation with the grid in Fig. 2 together with a total integration time of $5 \cdot 10^{-15}$ s takes 151 s with the DGTD-$\mathcal{P}_1$ method. Increasing the polynomial order to 2 leads to a computational time of 945 s. As our code is

**Table 2**
Computational parameters for the simulation run $\mathcal{P}_1$ and $\mathcal{P}_2$.

| # cells | # dof ($\mathcal{P}_1$; $\mathcal{P}_2$) | RAM ($\mathcal{P}_1$; $\mathcal{P}_2$) [MB] | CPU | runtime ($\mathcal{P}_1$; $\mathcal{P}_2$) [s] |
|---------|------|------|-----|---------|
| 8816 | 26448; 52896 | 23; 27 | Intel®Xeon®CPU E5-1620 v2, 3.70 GHz | 151, 945 |
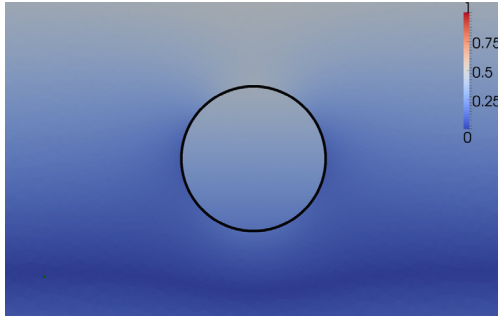


(a) Fourier transformed field plot of $|E_x|$ computed with DGTD-$\mathcal{P}_1$ for the local Drude model. The surface plasmon mode is observable. Also, the mode can penetrate into the dispersive regime because $\omega_{c,2}$ is higher than the plasma frequency.
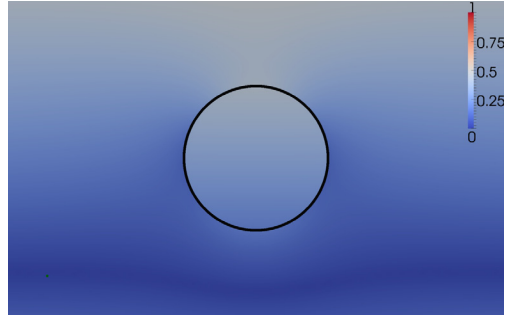
(b) Fourier transformed field plot of $|E_x|$ computed with DGTD-$\mathcal{P}_2$ for the local Drude model. The solution is slightly smoother compared to DGTD-$\mathcal{P}_1$. However, the gain in accuracy is not too obvious.
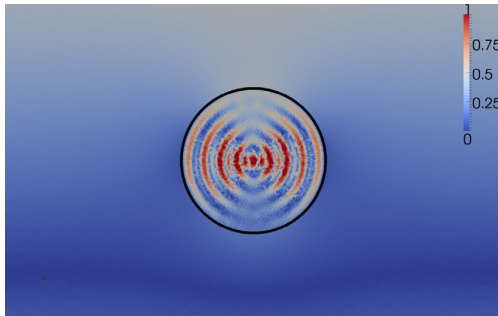
(c) Fourier transformed field plot of $|E_x|$ computed with DGTD-$\mathcal{P}_1$ for the non-local dispersion model. The fourth resonance of the bulk plasmon mode is observable.
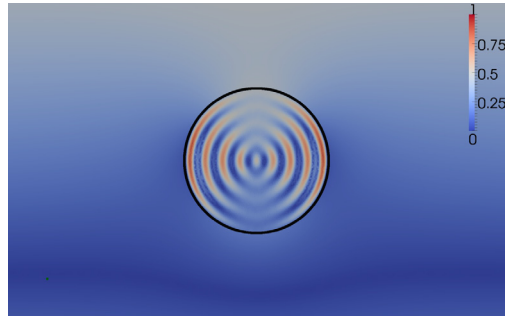
(d) Fourier transformed field plot of $|E_x|$ computed with DGTD-$\mathcal{P}_2$ for the non-local dispersion model. The solution in the dispersive regime is significantly smoother and the maximum amplitude is reduced by factor 2.5.

**Fig. 3.** Field solutions of a dispersive nanodisk with a radius of 2 nm. The plots show the Fourier transformed time domain solution of $|E_x|$ for the local and non-local dispersion model. All computations were done for $\omega_{c,2} = 1.1963\omega_p$ for DGTD-$\mathcal{P}_1$ and DGTD-$\mathcal{P}_2$, respectively.

designed for the non-local model, local Drude solution can be obtained by setting $\beta = 0$. Thus, computations for the local and non-local cases show the same computational time. It may be mentioned that the implementation is neither optimized nor parallelized. This will be done for the 3D case in a future work. However, the gain in accuracy for DGTD-$\mathcal{P}_2$ is obvious even for a rather coarse mesh compared to the wavelength of the bulk plasmon. Further, possible improvements would be PML boundary conditions [48] or curvilinear elements [49]. The important influence of curvilinear elements in the context of nanophotonic computations has been also demonstrated in [50].

### 4.3.1. Physical discussion

We now want to have a look on the physical interpretation of the computed results. The following computations were all done with the DGTD-$\mathcal{P}_2$ method and the same parameters as above. We basically compare the results for the local Drude model with the non-local hydrodynamic model. For the angular frequency $\omega_{c,1}$, we would expect small differences between both models. As this frequency is below the plasma frequency, only surface plasmons can be excited. Fig. 4 shows

**Table 3**
Physical parameters for the hydrodynamic model. $\omega_c^1$ and $\omega_c^2$ are the two central frequencies of the excitation signal.

| $\omega_p$ | $\gamma_c$ | $\beta$ | $\omega_{c,1}/\omega_p$ | $\omega_{c,2}/\omega_p$ |
|---|---|---|---|---|
| $13.39 \cdot 10^{15}$ rad/s | $0.1143 \cdot 10^{15}$ rad/s | $1.1349 \cdot 10^6$ m/s | 0.6503 | 1.1963 |

**Table 4**
Simulation parameters of the illuminating field for the runs below and above the plasma frequency. Here, the subscript $i$ links $\alpha_i$ to the computational run with $\omega_{c,i}$, for $i = 1, 2$.

| $T_{max}$ | $\alpha_1$ | $\alpha_2$ | $\tau_1$ | $\tau_2$ |
|---|---|---|---|---|
| $5 \cdot 10^{-15}$ s | $2 \cdot 10^{-16}$ s | $1 \cdot 10^{-16}$ s | $1 \cdot 10^{-17}$ s | $1 \cdot 10^{-17}$ s |
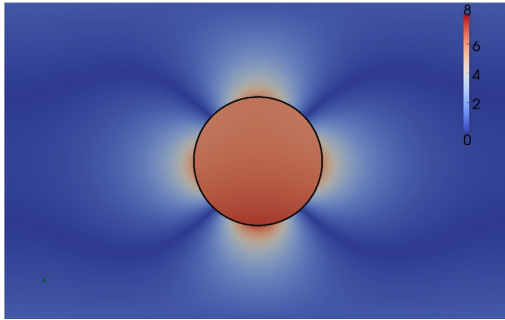


(a) $|E_x|$ for the local Drude model. The localized plasmon resonance is clearly visible. The discontinuity of this component of the electric field is located at the edges of the metal due to the interface conditions.
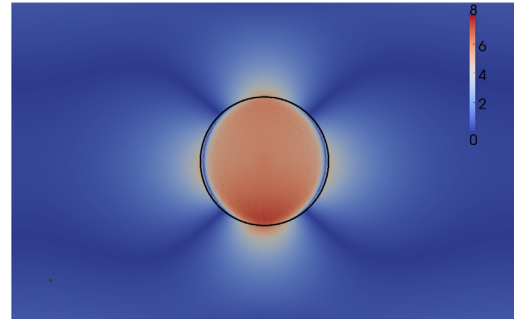
(b) $|E_x|$ for the non-local dispersion model. Here, the interface conditions change due to the non-local model and hence displace and smear out the discontinuity of $|E_x|$ towards the center.
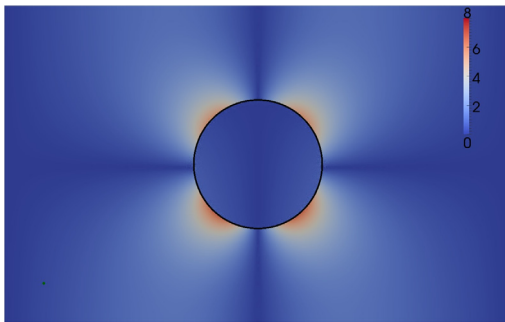
(c) $|E_y|$ for the local Drude model. It is literally pushed out of the metal due to the interface conditions.
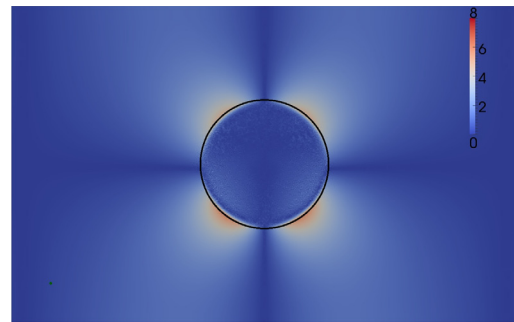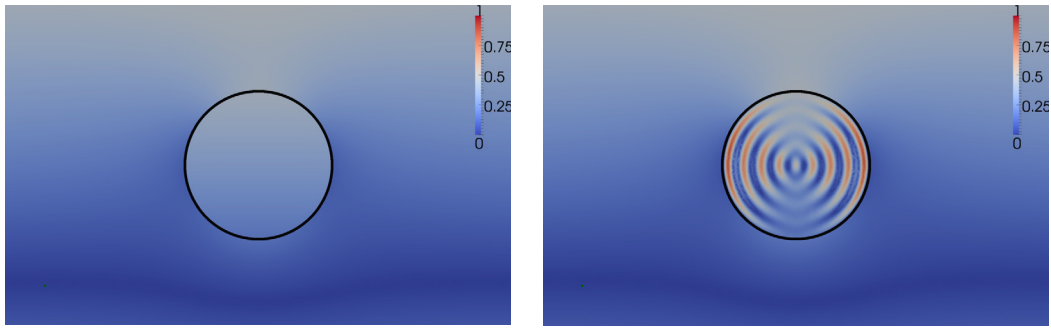
(d) $|E_y|$ for the non-local dispersion model. The non-local behavior and the corresponding interface conditions allow a deeper penetration with respect to the local Drude model.

**Fig. 4.** Field solutions of a dispersive nanodisk with a radius of 2 nm. The four figures show the Fourier transformed field solutions of $|E_x|$ and $|E_y|$ for the local and non-local dispersion model. All computations were done with DGTD-$\mathcal{P}_2$ at $\omega_{c,1}$.

the Fourier transformed field solutions for the $E_x$ and $E_y$ component. Both field patterns have more or less the same shape. However, the local model allows a very small penetration that is almost not visible. In contrast, the non-local solution makes penetration easier and we can see the strongest penetration in the direction of the incident field polarization. This is fairly reasonable since the plasmon gets excited due to the electric field. In other words, the electrons get *pushed* by the incident field. We want to emphasize that the shown field distributions correspond to the absolute value of the discrete Fourier transform. What seems to be a quadrupole field is in reality a dipole field.

Let us switch to the second angular frequency $\omega_{c,2}$ that is clearly above the plasma frequency and corresponds to the fifth bulk plasmon resonance according to the cross-section calculations in [31]. Fig. 5 shows the obtained field plots. In

(a) $|E_x|$ for the local Drude model. No resonance can be clearly observed. Since the frequency is above the plasma frequency the metal increases its transparency for the electromagnetic wave.

(b) $|E_x|$ for the non-local dispersion model. Bulk plasmons are excited inside the disk due to the non-locality. The fifth order resonance is shown here.
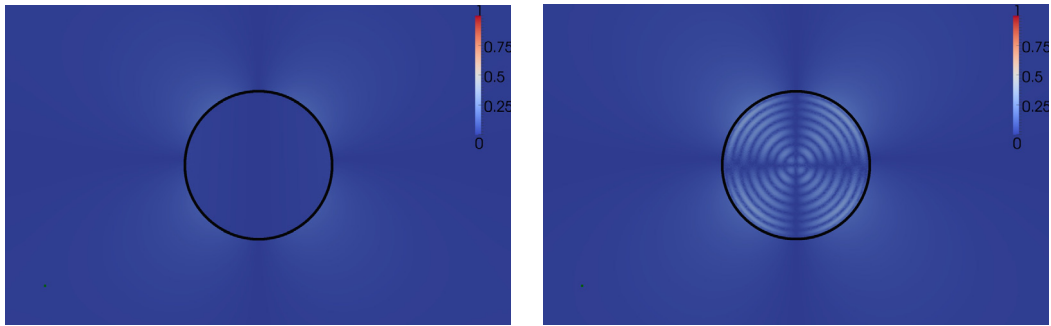
(c) $|E_y|$ for the local Drude model. The metal is equally transparent as for $|E_x|$.

(d) $|E_y|$ for the non-local dispersion model. Bulk plasmons are excited inside the disk due to the non-locality.

**Fig. 5.** Field solutions of a dispersive nanodisk with a radius of 2 nm. The four figures show the Fourier transformed field solutions of $|E_x|$ and $|E_y|$ for the local and non-local dispersion model. All computations were done with DGTD-$\mathcal{P}_2$ at $\omega_{c,2}$.

case of the local approximation, no resonance seems to be excited in the structure. In contrast, the non-local model shows a completely different pattern which we interpret as a bulk plasmon resonance. This bulk plasmon is mostly excited where the metal surface is perpendicular to the incident electric field polarization. Consequently, the resonance pattern is essentially perpendicular to the propagation direction of the incident plane wave.

All these results are thus in accordance with the discussion in [31]. We also observed new resonances in the non-local model that do not exist in the local one. Also, similar field patterns of the linear contribution in a non-linear simulation have been observed in [43]. The interested reader is also referred to [33] to find a detailed discussion on the central point of [31] that we choose not to recall here. As a last remarkable result, we want to have a look at the scattered field due to the excited resonances. The most appropriate way to study the resonance behavior of a nanostructure is to evaluate the cross section which is a spectral quantity. This will be considered in a subsequent work and we propose here to stick to the time-domain viewpoint. Indeed, it is still possible to observe the time evolution of the electromagnetic field at a determined point in the computational domain. In our case, the field monitor was placed at the point $(x, y) = (0\ \text{m},\ 4.5 \cdot 10^{-10}\ \text{m})$ for the $E_x$ component of the electric field. Fig. 6 shows the observed results. The blueshift of the surface plasmonic response for the non-local model is clearly observable and thus agrees with discussions in [9] and [31].

## 5. Conclusions

We have presented the first study of a DGTD method for the numerical solution of a linearized version of a non-linear hydrodynamic modeling of the electron gas for metals in the context of nanophotonics. As a matter of fact, the resulting coupled problem of Maxwell's equations together with the non-local dispersion model is still hyperbolic and the total energy is either preserved or decreasing if non-elastic collisions are modeled.

The spatial discretization of the coupled system with the DG method leads to a stable semi-discrete scheme. Discretizing this semi-discrete scheme in time with a second order leap-frog scheme, finally yields a non-dissipative fully-discrete formulation which is stable under a CFL type criterion.
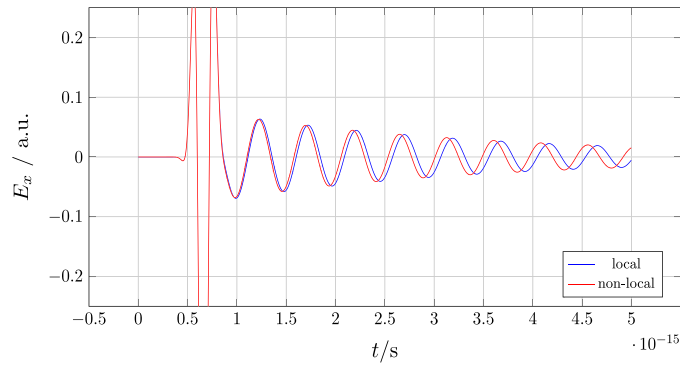
**Fig. 6.** $E_x$ component of the electric field at the point $(x, y) = (0\ \text{m},\ 4.5 \cdot 10^{-10}\ \text{m})$. The excitation signal is almost zero after $t = 1 \cdot 10^{-15}$ s and only the emitted field due to the excited plasmon can be observed. A blueshift of the resonance frequency w.r.t. the local model can be observed for the non-local model.

In order to verify our 2D implementation, we first considered a rather unphysical test case that allowed a verification of the spatial discretization. After having successfully tested the implementation, we considered an infinitely long nanowire as a physical test case. The computed time domain solutions were Fourier transformed and compared to frequency domain solutions afterwards. Our results show a good agreement with earlier published articles.

With this code, a first finite element time domain solver for the linearized hydrodynamic model is available permitting the illumination of 2D structures with arbitrarily shaped time signals. Although frequency domain solvers are generally able to treat arbitrarily shaped time signals, the computational costs increase dramatically for very short pulses and thus time domain algorithms are more appropriate. This allows new insights into the behavior of nano particles.

This work provides a first study of this model in the time domain within a DGTD framework and paves the way to the realization of more physical test cases and cross disciplinary works. Recent works have shown that many more structures than previously thought may be sensitive to non-local effects. Some present very complex geometries [51,52] and their study would undoubtedly profit from an efficient DGTD treatment. Future work will extend the present results in several directions. We will first propose more sophisticated posttreatment tools in a near future. Implementing non-linear hydrodynamic approaches that are essential to understand harmonic generation [53] is another direction.

Also, from a more numerical point of view, a 3D implementation, curvilinear elements, parallelization or higher order time integration schemes are natural paths for future works.

## Acknowledgements

## References

[1] G. Akselrod, C. Argyropoulos, T. Hoang, C. Ciracì, C. Fang, J. Huang, D. Smith, M. Mikkelsen, Probing the mechanisms of large Purcell enhancement in plasmonic nanoantennas, Nat. Photonics 8 (11) (2014) 835–840.
[2] J. Schuller, E. Barnard, W. Cai, Y. Jun, J. White, M. Brongersma, Plasmonics for extreme light concentration and manipulation, Nat. Mater. 9 (3) (2010) 193–204.
[3] A. Moreau, C. Ciracì, J. Mock, R. Hill, Q. Wang, B. Wiley, A. Chilkoti, D. Smith, Controlled-reflectance surfaces with film-coupled colloidal nanoantennas, Nature 492 (7427) (2012) 86–89.
[4] G. Akselrod, T. Ming, C. Argyropoulos, T. Hoang, Y. Lin, X. Ling, D. Smith, J. Kong, M. Mikkelsen, Leveraging nanocavity harmonics for control of optical processes in 2D semiconductors, Nano Lett. 15 (5) (2015) 3578–3584.
[5] N. Crouseilles, P.A. Hervieux, G. Manfredi, Quantum hydrodynamic model for the nonlinear electron dynamics in thin metal films, Phys. Rev. B 78 (2008) 155412.
[6] C. Ciracì, R. Hill, J. Mock, Y. Urzhumov, A. Fernández-Domínguez, S. Maier, J. Pendry, A. Chilkoti, D. Smith, Probing the ultimate limits of plasmonic enhancement, Science 337 (6098) (2012) 1072–1074.
[7] C. Ciracì, X. Chen, J. Mock, F. McGuire, X. Liu, S. Oh, D. Smith, Film-coupled nanoparticles by atomic layer deposition: comparison with organic spacing layers, Appl. Phys. Lett. 104 (2) (2014) 023109.
[8] A. Moreau, C. Ciraci, D. Smith, Impact of nonlocal response on metallodielectric multilayers and optical patch antennas, Phys. Rev. B 87 (045401-1–045401-11) (2013) 6795–6820.
[9] T. Christensen, W. Yan, S. Raza, A. Jauho, N.A. Mortensen, M. Wubs, Nonlocal response of metallic nanospheres probed by light, electrons, and atoms, ACS Nano 8 (2) (2014) 1745–1758.
[10] S. Bozhevolnyi, T. Søndergaard, General properties of slow-plasmon resonant nanostructures: nano-antennas and resonators, Opt. Express 15 (17) (2007) 10869–10877.
[11] S. Raza, T. Christensen, M. Wubs, S. Bozhevolnyi, N. Mortensen, Nonlocal response in thin-film waveguides: loss versus nonlocality and breaking of complementarity, Phys. Rev. B 88 (11) (2013) 115401.

[12] M. Dechaux, P.-H. Tichit, C. Ciracì, J. Benedicto, R. Pollès, E. Centeno, D. Smith, A. Moreau, Influence of spatial dispersion in metals on the optical response of deeply subwavelength slit arrays, Phys. Rev. B 93 (4) (2016) 045413.

[13] K. Savage, M. Hawkeye, R. Esteban, A. Borisov, J. Aizpurua, J. Baumberg, Revealing the quantum regime in tunnelling plasmonics, Nature 491 (7425) (2012) 574–577.

[14] R. Esteban, A. Borisov, P. Nordlander, Bridging quantum and classical plasmonics with a quantum-corrected model, Nat. Commun. 3 (825) (2012) 1–9.

[15] G. Toscano, J. Straubel, A. Kwiatkowski, C. Rockstuhl, F. Evers, H. Xu, N. Mortensen, M. Wubs, Resonance shifts and spill-out effects in self-consistent hydrodynamic nanoplasmonics, Nat. Commun. 6 (2015) 7132.

[16] J. Niegemann, Higher-order methods for solving Maxwell's equations in the time-domain, Ph.D. thesis, Fakultät für Physik des Karlsruher Instituts für Technologie, 2009.

[17] J. Hesthaven, T. Warburton, Nodal high-order methods on unstructured grids, I: time-domain solution of Maxwell's equations, J. Comput. Phys. 181 (1) (2002) 186–221.

[18] J. Li, J. Hesthaven, Analysis and application of the nodal discontinuous Galerkin method for wave propagation in metamaterials, J. Comput. Phys. 258 (2014) 915–930.

[19] K. Busch, M. König, J. Niegemann, Discontinuous Galerkin methods in nanophotonics, Laser Photonics Rev. 5 (2011) 1–37.

[20] T. Lu, W. Cai, P. Zhang, Discontinuous Galerkin methods for dispersive media and lossy Maxwell's equations and PML boundary conditions, J. Comput. Phys. 200 (2004) 549–580.

[21] J. Niegemann, R. Diehl, K. Busch, Efficient low-storage Runge–Kutta schemes with optimized stability regions, J. Comput. Phys. 231 (2) (2012) 364–372.

[22] X. Ji, W. Cai, P. Zhang, High-order DGTD method for dispersive Maxwell's equations and modelling of silver nanowire coupling, Int. J. Numer. Methods Eng. 69 (2007) 308–325.

[23] S. Gedney, J. Young, T. Kramer, J. Roden, A discontinuous Galerkin finite element time-domain method modeling of dispersive media, IEEE Trans. Antennas Propag. 60 (4) (2012) 1969–1977.

[24] S. Lanteri, C. Scheid, Convergence of a discontinuous Galerkin scheme for the mixed time domain Maxwell's equations in dispersive media, IMA J. Numer. Anal. 33 (2) (2013) 432–459.

[25] J. Li, Y. Chen, V. Elander, Mathematical and numerical study of wave propagation in negative-index material, Comput. Methods Appl. Mech. Eng. 197 (2008) 3976–3987.

[26] J. Li, Numerical convergence and physical fidelity analysis for Maxwell's equations in metamaterials, Comput. Methods Appl. Mech. Eng. 198 (2009) 3161–3172.

[27] L. Fezoui, S. Lanteri, S. Lohrengel, S. Piperno, Convergence and stability of a discontinuous Galerkin time-domain method for the 3D heterogeneous Maxwell equations on unstructured meshes, ESAIM: Math. Model. Numer. Anal. 39 (6) (2005) 1149–1176.

[28] J. Viquerat, S. Lanteri, C. Scheid, Theoretical and numerical analysis of local dispersion models coupled to a discontinuous Galerkin time-domain method for Maxwell's equations, Tech. rep. 8298, INRIA, 2013, https://hal.inria.fr/.

[29] K. Hiremath, L. Zschiedrich, F. Schmidt, Numerical solution of nonlocal hydrodynamic Drude model for arbitrary shaped nano-plasmonic structures using Nedelec finite elements, J. Comput. Phys. 231 (2012) 5890–5896.

[30] G. Toscano, S. Raza, A.-P. Jauho, N.A. Mortensen, M. Wubs, Modified field enhancement in plasmonic nanowire dimers due to nonlocal response, Opt. Express 20 (4) (2011) 4176–4188.

[31] S. Raza, G. Toscano, A.-P. Jauho, M. Wubs, N.A. Mortensen, Unusual resonances in nanoplasmonic structures due to nonlocal response, Phys. Rev. B 84 (2011) 121412.

[32] Q. Huang, F. Bao, S. He, Nonlocal effects in a hybrid plasmonic waveguide for nanoscale confinement, Opt. Express 21 (2) (2013) 1430–1439.

[33] N. Schmitt, C. Scheid, S. Lanteri, A. Moreau, J. Viquerat, A DGTD method for the numerical modeling of the interaction of light with nanometer scale metallic structures taking into account non-local dispersion effects, Tech. rep. 8726, INRIA, 2015, https://hal.inria.fr/.

[34] J. Jackson, Classical Electrodynamics, John Wiley & Sons, 1999.

[35] C. Kittel, Introduction to Solid State Physics, 8th edition, Wiley, 2004.

[36] M. Stockmann, Nanoplasmonics: the physics behind the applications, Phys. Today 64 (2) (2011) 39–44.

[37] T. Teperik, P. Nordlander, J. Aizpurua, A. Boriso, Quantum plasmonic: nonlocal effects in coupled nanowire dimer, Opt. Express 21 (22) (2013) 27306–27325.

[38] S. Maier, Plasmonics – Fundamentals and Applications, Springer, 2007.

[39] N.A. Mortensen, Nonlocal formalism for nanoplasmonics: phenomenological and semi-classical considerations, Photonics Nanostruct. Fundam. Appl. 11 (4) (2013) 303–309.

[40] F. Chen, Introduction to Plasma Physics and Controlled Fusion: Plasma Physics, Springer, 2006.

[41] C. David, N.A. Mortensen, J. Christensen, Perfect imaging, epsilon-near zero phenomena and waveguiding in the scope of nonlocal effects, Sci. Rep. 3 (2526) (2013) 1–7.

[42] A. Boardman, Electromagnetic Surface Modes, John Wiley & Sons, 1972.

[43] A. Hille, M. Moeferdt, C. Wolff, C. Matyssek, R. Roderigez-Oliveros, C. Prohm, J. Niegemann, S. Grafström, L. Eng, K. Busch, Second harmonic generation form metal nano-particle resonators: numerical analysis on the basis of the hydrodynamic Drude model, J. Phys. Chem. C 120 (2016) 1163–1169.

[44] W. Reed, T. Hill, Triangular mesh methods for the neutron transport equation, Tech. rep. 479, Los Alamos Scientific Laboratory, 1973.

[45] J. Hesthaven, T. Warburton, Nodal Discontinuous Galerkin Methods: Algorithms, Analysis and Applications, Springer Texts in Applied Mathematics, Springer Verlag, 2007.

[46] K. Yee, Numerical solution of initial boundary value problems involving Maxwell's equations in isotropic media, IEEE Trans. Antennas and Propag. 14 (3) (1966) 302–307.

[47] S. Brenner, R. Scott, The Mathematical Theory of Finite Element Methods, Springer, 2008.

[48] J. Niegemann, M. König, K. Stannigel, K. Busch, Higher-order time-domain methods for the analysis of nano-photonic systems, Photonics Nanostruct. Fundam. Appl. 7 (2009) 2–11.

[49] T. Warburton, A low storage curvilinear discontinuous Galerkin time-domain method for electromagnetics, in: 2010 URSI International Symposium on Electromagnetic Theory, EMTS, IEEE Xplore, Berlin, 2010, pp. 996–999.

[50] R. Kullock, M. Hille, A. Haussmann, S. Grafström, L. Eng, SHG of plasmonic nano-particles using curved elements, Opt. Express 19 (2011) 14426–14436.

[51] A. Wiener, A. Fernàndez-Domínguez, A. Horsfield, J. Pendry, S. Maier, Nonlocal effects in the nanofocusing performance of plasmonic tips, Nano Lett. 12 (6) (2012) 3308–3314.

[52] A. Wiener, H. Duan, M. Bosman, A. Horsfield, J. Pendry, J. Yang, S. Maier, A. Fernàndez-Domínguez, Electron-energy loss study of nonlocal effects in connected plasmonic nanoprisms, ACS Nano 7 (7) (2013) 6287–6296.

[53] C. Ciracì, M. Scalora, D. Smith, Third-harmonic generation in the presence of classical nonlocal effects in gap-plasmon nanostructures, Phys. Rev. B 91 (2015) 205403.